Two-mica rhyolitic tephra in the East Pisco Basin (Peru): new age and dispersion constraints for the eruptions of the Eastern Cordillera of Central Andes

Giulia Bosio*[1,2], Anna Gioncada[1], Claudio Di Celma[3], Igor Maria Villa[2,4,5], Michael Pichavant[6], Mario Urbina[7], Giovanni Bianucci[1]

[1] Dipartimento di Scienze della Terra, Università di Pisa, 56126 Pisa, Italy. giulia.bosio.giulia@gmail.com; anna.gioncada@unipi.it; giovanni.bianucci@unipi.it

[2] Dipartimento di Scienze dell'Ambiente e della Terra, Università degli Studi di Milano-Bicocca, 20126 Milano, Italy. giulia.bosio.giulia@gmail.com; igor.villa@unimib.it

[3] Scuola di Scienze e Tecnologie, Università di Camerino, 62032 Camerino, Italy. claudio.dicelma@unicam.it

[4] Institut für Geologie, Universität Bern, 3012 Bern, Switzerland. igor.villa@geo.unibe.ch

[5] Centro Universitario Datazioni e Archeometria, Università degli Studi di Milano-Bicocca, 20126 Milano, Italy. igor.villa@unimib.it

[6] Université d'Orléans/CNRS/ISTO/BRGM, UMR 7327, 1A rue de la Férollerie, 45100 Orléans, France. pichavan@cnrs-orleans.fr[7] Departamento de Paleontología de Vertebrados, Museo de Historia Natural, Universidad Nacional Mayor de San Marcos, Lima 1, Peru. mariourbina01@hotmail.com

*corresponding author: giulia.bosio.giulia@gmail.com; +390502215700

Key words

Strongly peraluminous tephra, ^{39}Ar–^{40}Ar ages, Miocene, Central Andes, Macusani, Morococala

Abstract

Two-mica - biotite and muscovite - volcanics are particularly rare in the geological record. One of the several dozen volcanic ash layers from Central Andes volcanoes found in the upper Miocene marine succession of the Pisco Formation (Ica Desert, Peru) contains juvenile biotite and muscovite, sillimanite/andalusite, feldspars and rhyolitic glass. ^{39}Ar–^{40}Ar dating on biotite and muscovite concordantly constrain an age of 7.96 Ma for this two-mica ash layer. A second tephra in the Pisco Formation has a similar biotite composition and an age between 7.45 and 6.93 Ma. The peculiar mineral assemblage and the chemical composition of biotite indicate a strongly peraluminous composition of the erupted magmas and, together with the ^{39}Ar–^{40}Ar ages, suggest to consider a correlation of these ash layers to the eruptions of the Miocene Macusani (Peru) or Morococala (Bolivia) volcanic complexes in the Eastern Cordillera of Central Andes. The major and trace element composition of glass supports the correlation with Macusani. A provenance from Morococala seems less likely given the large distances involved. These results provide new data on the volcanic activity of the Eastern Cordillera revealing ash that dispersed to over 500 km to the west, in the forearc marine basins. This finding highlights that the exhumed forearc East Pisco Basin is highly promising as an archive of distal ash for the reconstruction of the volcanic activity of Central Andes during the Miocene silicic flare-ups.

Introduction

Strongly peraluminous (SP) volcanics (in the sense of Miller 1985: Al_2SiO_5-, two mica-, garnet- or cordierite bearing “granitic” rocks) are particularly rare in the geological record. One of the largest peraluminous volcanic provinces is in the Eastern Cordillera of the Central Andes. Here, tectono-magmatic conditions responsible for generating crustal melts of strongly peraluminous composition prevailed for several million years in late Miocene (Sandeman et al. 1997; Caffe et al. 2012). Although the Cenozoic marine sediments of the offshore and emerged forearc basins of southern Peru host many tuff layers representing distal volcanic ash of Central Andes eruptions, dispersed

52 westwards by easterly winds (Pouclet et al. 1990; Hart and Miller 2006; Bosio et al. 2019), no
53 correlations with the Eastern Cordillera activity have been proposed up to now.
54 In the East Pisco Basin (southern Peru), the Miocene Pisco Formation hosts many
55 undisturbed volcanic ash layers in diatomaceous sedimentary successions (Di Celma et al. 2017;
56 Bosio et al. 2020b). Most of them, based on glass and biotite composition and mineral assemblage,
57 are calcalkaline dacites and rhyolites and subordinate andesites (Bosio et al. 2019) representing the
58 subduction-related activity of the Western Cordillera (Mamani et al. 2010). A few, instead, show
59 biotite composition pointing to the siderophyllite end-member, suggesting a peraluminous nature of
60 the erupted magma (Bosio et al. 2019). One of these latter ash layers is a two-mica - biotite and
61 muscovite - rhyolitic tephra.
62 In this paper, we provide field and petro-chemical descriptions of volcanic ash and age
63 determinations and discuss the possible finding of Eastern Cordillera ash in the forearc East Pisco
64 Basin. These results add new information about the volcanic activity of the Eastern Cordillera of
65 Central Andes and reveal two major eruptions of strongly peraluminous magmas at 7–8 Ma that
66 dispersed volcanic products up to hundreds of kilometers to the west, reaching the coastal forearc
67 basins.
68
69 **Geological and volcanological framework**
70 Since the Mesozoic, the western margin of South America has been influenced by the subduction of
71 the oceanic Nazca/Farallon Plate underneath the continental South American Plate. In the Central
72 Andes, this subduction was responsible for the production of calc-alkaline metaluminous magmas
73 along the western magmatic arcs forming the Western Cordillera (Baker and Francis 1978; de Silva
74 and Francis 1991; Trumbull et al. 2006; Mamani et al. 2010). On the eastern side of the Central
75 Andes orogen, instead, the peraluminous and S-type volcanic and intrusive magmatic units
76 emplaced since 25 Ma indicate that the Eastern Cordillera magmatism is not related to subduction
77 and was the result of extensive crustal melting (Trumbull et al. 2006). Confirming this petrogenetic

distinction, the extensive fractional crystallization of the Eastern Cordillera crustal-derived magmas led to Sn and W enrichment (Mlynarczyk and Williams-Jones 2005), while in the western Cordillera, predominantly mantle-derived, metaluminous magmas led to porphyry Cu-Au-Mo and epithermal ore deposits (Rosenbaum et al. 2005). Examples of the crustal-derived magmatic units of the Eastern Cordillera emplaced from 14° S to 26°S (see Fig. 1) are the Kari Kari ignimbrite (Schneider 1987), the Macusani volcanics (Noble et al. 1984; Pichavant et al. 1988a, b), the Morococala Meseta ignimbrites (Morgan et al. 1998), Revancha dyke (Sandeman and Clark 2003), Cayconi volcanic field (Sandeman and Clark 2004), and Los Frailes ignimbrites (Kay et al. 2010).

Volcanic ash layers linked to the activity of the Central Andes (Central Volcanic Zone) have been found along the Peruvian and Chilean coast (Pouclet et al. 1990; Hart and Miller 2006; Breitkreutz et al. 2014; Bosio et al. 2019), in the Coastal Cordillera and in the forearc basins formed during the Cenozoic (Travis et al. 1976; Thornburg and Kulm 1981). These products represent the distal ash of large explosive eruptions, which may have been dispersed westwards by south-southeasterly winds, similar to the products of the Huaynaputina eruption, the largest explosive event in historical times (1600 AD) in Peru (Thouret et al. 1997; de Silva and Zielinski 1998). One of the forearc basins, the East Pisco Basin now exposed in the Ica Desert of Peru, hosts one of the most world-renowned marine vertebrate Fossil-Lagerstätte (Esperante et al. 2015; Bianucci et al. 2016a, b, 2018).

The Miocene Pisco Formation is the youngest unit of the East Pisco Basin marine fill and is mainly composed of diatomaceous siltstones and sandstones, interposed by frequent tephra layers (Dunbar et al. 1990). Di Celma et al. (2017) divided this formation in three main allomembers, P0, P1 and P2, from the oldest to the youngest, bounded by regionally extensive intraformational unconformities. Each allomember is composed of yellow sandstones at the base and white diatomaceous siltstone at the top. Along the western side of the Ica River, the P0 allomember was deposited in between 14.8 and 12.4 Ma (Bosio et al. 2020a), the P1 allomember between 9.5 and 8.6 Ma, whereas the P2 allomember was deposited from 8.4 to at least 6.7 Ma (Bosio et al. 2020b).

104 Volcanic ash layers are mainly preserved in the diatomaceous mudstone portions of the marine
105 successions of the P1 and P2 allomembers.
106
107 **Methods**
108 Among more than 200 samples of volcanic ash layers collected in the East Pisco Basin succession
109 during the fieldwork from 2014 to 2016, this work focuses on three ash samples from the localities
110 of Cerros la Mama y la Hija, Cerro los Quesos and Cerro la Bruja (Fig. 2). Samples were collected
111 at the base of the ash layer in order to avoid any possible reworking and bioturbation affecting the
112 top of the layer. The surface of the outcrop was discarded to avoid weathered or extraneous grains.
113 Before compositional and ^{39}Ar–^{40}Ar dating analyses, the samples were inspected under a
114 stereomicroscope and smear slides were studied under an optical microscope for petrographic
115 features. The ash layers were considered as the primary deposition of tephra on the basis of a
116 percentage of volcanic components (glass shards and juvenile loose crystals) greater than 95 vol%
117 (Griggs et al. 2014; Tada et al. 2015).
118 Grain-size analyses were performed with the Malvern Mastersizer 2000E™ Laser
119 Granulometer and processed with the Grain Size Analysis Program GRADISTAT (Blott and Pye
120 2001) at the Università di Milano-Bicocca (Dipartimento di Scienze dell'Ambiente e della Terra,
121 Milano, Italy). The ash samples were wet sieved with meshes of 500, 250, 125 and 63 μm, and the
122 125–250 μm and 250–500 μm fractions were mounted in resin and polished for compositional
123 analyses. SEM-EDS (scanning electron microscope equipped with electron dispersion
124 spectroscopy) microanalysis was carried out at the Università di Pisa (Dipartimento di Scienze della
125 Terra, Pisa, Italy) with a Philips™ XL30 scanning electron microscope equipped with an Edax
126 Genesis microanalytical device, with 20 kV filament voltage, 5 nA beam current and ZAF
127 correction. EPMA (Electron Probe Micro-Analysis) analyses for major elements were performed on
128 glass shards, Al-Si minerals, biotite and muscovite phenocrysts with a JEOL 8200 Superprobe™ at
129 the Università di Milano (Dipartimento di Scienze della Terra "Ardito Desio", Milano, Italy) (15 kV

accelerating voltage, 5 nA beam current) with counting time of 30 s on the elemental peak and 10 s on the background. The beam diameter was 3 μm for phenocrysts and 10 μm for glass shards, i.e. enlarged in order to avoid Na migration under the beam. EPMA analyses were also performed for major elements, zinc and fluorine at the Institut des Sciences de la Terre d'Orleans (ISTO) (Orléans, France) facilities with a SX Five CAMECA instrument, with 15 kV accelerating voltage and 5 nA beam current. The counting time was 10 s on peak and 5 s on background; the spot size was defocused to 10 μm on glasses and focused to 1-2 μm on minerals.

Trace element concentrations in the MH-T4 matrix glass were analyzed by LA-ICP-MS at Orléans (joint ISTO-IRAMAT facility). A RESOlution ArF excimer laser (LA; λ=193 nm) coupled to an Agilent TripleQuad ICPMS was used. Ablation was performed at a frequency of 10 Hz and an energy of 2.5 $J.cm^{-2}$. A beam diameter of 10 μm was used. NIST610 was used as external standard and obsidian glass JV2 (Pichavant et al. 1987) as secondary standard. Since small spot sizes were necessary, systematic analyzes were performed on JV2 at different spot sizes between 100 to 10 μm to check that decreasing spot sizes had no significant effect on element concentrations. A total of three successful analyzes were obtained. The raw data were processed off-line using the Glitter software (Griffin 2008) where time-resolved signals were examined one by one.

For ^{39}Ar–^{40}Ar analysis, biotite and muscovite phenocrysts were carefully hand-picked under a stereomicroscope, making particular care to avoid any contamination, following Bosio et al. (2020b). ^{39}Ar–^{40}Ar dating were performed with the NuInstruments™ Noblesse® noble gas mass spectrometer at the Università di Milano-Bicocca using the step-heating procedure described by Bosio et al. (2020b).

Results

Field and petrographic description

The sample MH-T4 was collected from an ash layer outcropping at Cerros la Mama y la Hija (Fig. 2, 3), at the base of the P2 allomember, 3 m above the PE0.2 unconformity (Fig. 3). The layer is a 5

156 cm-thick white ash with visible fine biotite, which can be traced laterally for several tens of meters
157 in sandstones. The CLQ-T23 and LB-T19 ash layers were sampled in Cerro los Quesos and Cerro la
158 Bruja localities, respectively (Fig. 2). These ash layers were described and correlated based on
159 stratigraphy, grain-size, shard morphology and glass and biotite composition by Bosio et al. (2019)
160 and they will be referred to as CLQ-T23/LB-T19 tephra herein after.
161 Under the optical microscope, the MH-T4 ash consists of highly vesiculated, colorless glass
162 shards and of loose crystals of juvenile biotite, feldspars and minor muscovite. An Al_2SiO_5 mineral
163 phase, andalusite or sillimanite, was also detected inspecting the sample with SEM-EDS (Fig. 4).
164 Biotite, muscovite, feldspar and andalusite/sillimanite are coated by juvenile rhyolitic glass (Fig. 4).
165 The CLQ-T23/LB-T19 tephra consists of colorless glass shards with a bubble-wall morphology and
166 only a very few small phenocrysts of biotite. Through grain-size analysis, we find that both tephra
167 samples are unimodal and poorly sorted (see Fig. 4e), and they are composed by extremely fine ash
168 (<1/16 mm) following the classification of White and Houghton (2006).
169
170 ***Mineral and glass composition***
171 Biotite phenocrysts of both tephra layers (MH-T4 and CLQ-T23/LB-T19) show a rather
172 homogeneous major element composition from core to rim (Tables 1a, 1b). From the point of view
173 of the biotite classification in an Al^{IV} vs Fe/Fe+Mg diagram, they are on the siderophyllite-rich side
174 of the field representing the composition of biotite found in the P2 allomember tephra (Fig. 5a).
175 Biotite composition, for both tephra layers, can be distinguished from the rest of the P2 tephra in Ti
176 vs Fe/Fe+Mg (Fig. 5b). Moreover, biotite phenocrysts are richer in Al_2O_3 wt% with respect to the
177 rest of P2 tephra (Fig. 5c) and fall within the field of the micas found in peraluminous granite in the
178 discrimination diagrams of Abdel-Rahman (1994) (Fig. 5c, d). They show detectable ZnO contents
179 while F is mostly below detection (Tables 1a, 1b).
180 The peculiarity of the MH-T4 tephra is the presence of muscovite crystals, which are
181 juvenile phenocrysts as indicated by the coating of rhyolitic glass (Fig. 4c). Muscovite contains

182 significant amounts of Ti, Fe, and Mg, detectable ZnO and high F, similarly to muscovite in SP
183 rocks (Table 2). Feldspar phenocrysts coated by rhyolitic glass are both plagioclase (oligoclase) and
184 sanidine (Table 3, Fig. 5e). MH-T4 tephra shows, also, the presence of Al_2SiO_5 minerals in rhyolitic
185 glass, probably andalusite or sillimanite (Table 4).

186 The composition of the matrix glass is rhyolitic and, on the basis of K_2O vs. SiO_2 diagram,
187 corresponds to magmas belonging to the high-K calcalkaline series (Table 5, Fig. 6a). When
188 normalized to 100, the silica and CaO content is slightly higher and the Al_2O_3 is slightly lower for
189 MH-T4 than for CLQ-T23/LB-T19 (Fig. 6b, c). The low microprobe analysis totals may indicate
190 that hydration of glass occurred following the subaqueous deposition of ash. Since the removal of
191 mobile cations following interaction with an aqueous fluid may cause an increase of the A/CNK
192 (molar $Al_2O_3/CaO+Na_2O+K_2O$) ratio of glass, the analyses showing at the same time low K_2O, low
193 microprobe total and high A/CNK were discarded. The obtained A/CNK ratio of (mean value) 1.18
194 in MH-T4 and 1.28 in CLQ-T23/LB-T19 indicates a peraluminous composition (Fig. 6d).

195 The concentration of fluorine and of several trace elements were determined for MH-T4
196 matrix glasses. Fluorine is rather high (mean value of 2700 ppm, Table 5). The trace element
197 composition of the matrix glass normalized to Upper Continental Crust exhibits high B, Be, Rb, Cs,
198 Sn and low Li, Zr, Sr, Ba and La (Table 6, Fig. 6e).

199

200 ***^{39}Ar–^{40}Ar dating of the two-mica tephra***

201 The composition of MH-T4 biotite indicates a relatively high alkali site occupancy from 1.83 to
202 1.95 apfu, i.e. it is only slightly altered, which makes it suitable for ^{39}Ar–^{40}Ar dating. The K
203 concentration calculated from the ^{39}Ar release is substoichiometric. As discussed in more detail by
204 Bosio et al. (2020b), slight alteration affects micas from marine tephra.

205 The age spectrum of MH-T4 biotite shows a clear plateau (Fig. 7a). We consider only the
206 isochemical steps (sensu Villa et al. 2006), i.e. steps 2-6 having Ca/K < 0.005 and/or steps 3-6 with

207 Ca/K < 0.003 (see Fig. 7b). Both choices yield isochrons with an atmospheric intercept and a
208 slightly elevated MSWD = 3. The weighted average age of steps 2-6 is 7.98 ± 0.03 Ma.
209 The muscovite phenocrysts show a high alkali site occupancy, between 1.83 and 1.99 apfu,
210 reflecting a very slight alteration. The age spectrum of MH-T4 muscovite shows a plateau around 8
211 Ma (Fig. 7a). We chose the isochemical steps 3-9 with Ca/K < 0.005 and Cl/K < 0.00016 (Fig. 7b,
212 c). The isochron has an atmospheric intercept, therefore it is valid to consider the weighted average
213 age of steps 3-9, i.e. 7.95 ± 0.03 Ma. All the ^{39}Ar–^{40}Ar data for both the biotite and muscovite
214 separates are shown in Table 7 and Table 8, respectively.
215
216 **Discussion**
217 The East Pisco Basin tephra of the P2 allomember are prevalently rhyolitic for what concerns the
218 composition of glass shards (Bosio et al. 2019). The biotite composition of these tephra straddles
219 the phlogopite and biotite fields, with a trend pointing to the siderophyllite end-member (see Fig.
220 5a). When plotted in the discrimination diagrams for granitic rocks based on biotite composition
221 (Fig. 5c, d), they mostly fall in the field corresponding to mica in calcalkaline rocks, except for a
222 few falling in the field of mica in peraluminous rocks. Among these last tephra, one contains
223 juvenile muscovite, biotite and Al_2SiO_5 silicates, revealing a strongly peraluminous composition of
224 the erupted magma. The presence of this peculiar mineral association, unusual in subduction-related
225 arc system, leads to discuss the possible volcanic source for the ash.
226 Two-mica volcanic rocks are rare in the geological record and examples in upper Miocene
227 can be found in the Eastern Cordillera, which host one of the largest peraluminous provinces in the
228 world (Sandeman et al. 1997). In the Eastern Cordillera, the presence of volcanic muscovite has
229 only been reported in the Macusani and Morococala SP volcanic products (Noble et al. 1984;
230 Morgan et al. 1998). The Miocene-Pliocene Macusani ignimbrite field is the largest SP volcanic
231 unit in southern Peru (Noble et al. 1984; Pichavant et al. 1988a, b; Cheilletz et al. 1992). This field
232 comprises crystal-rich ash-flow tuffs and rare obsidian glasses, with an unusual mineralogy similar

233 to two-mica peraluminous leucogranites (Pichavant et al. 1987, 1988a). The Macusani Formation
234 consists of a 500 m-thick package of ash-flows of variable thickness, comprising six major cooling
235 units, which emplaced in two volcanic cycles, giving origin to a Lower and an Upper Member of
236 the formation (Cheilletz et al. 1992). In the Eastern Cordillera of Bolivia, the late Miocene
237 Morococala volcanic field is composed of andalusite-, biotite- and muscovite-bearing rhyolite tuffs
238 at the base, cordierite- and biotite-bearing rhyolite tuffs, and biotite-bearing quartz latite tuffs and
239 lavas at the top (Morgan et al. 1998).

240 A correlation with these Eastern Cordillera volcanics can be discussed on the basis of the
241 mineral assemblage and chemistry, glass composition, and age determinations. The chemical
242 composition of biotite, which has been demonstrated to be a useful tool for tephra correlations
243 (Shane et al. 2003; Lebti et al. 2006; Bosio et al. 2019), allows discriminating among the
244 peraluminous Central Andes volcanics (Caffe et al. 2012). The biotite composition of the MH-T4
245 and CLQ-T23/LB-T19 tephra layers corresponds well with analyses of mica of the Macusani and
246 Morococala SP volcanic units from previous work (i.e., Noble et al. 1984; Pichavant et al. 1988a, b;
247 Morgan et al. 1998), except for the low fluorine content (see Tables 1a, 1b; Fig. 5). In the case of
248 MH-T4 ash layer, the correlation is supported by the high F and the major and minor element
249 composition of muscovite, and by the composition of feldspar and Al-silicate minerals (Tables 2–
250 4).

251 To compare the glass composition of the Pisco tephra with the Macusani and Morococala
252 volcanics, the available data for matrix glasses and obsidian glasses (macusanite) from previous
253 work (Pichavant et al. 1987; London et al. 1988; Morgan et al. 1998) are reported in Table 5 and
254 Figure 6. A correlation with Macusani and Morococala volcanic regions is supported by the major
255 element composition of matrix glass and by the high F content measured on the MH-T4 glass
256 shards. The trace element composition of the ash glasses, with particularly high B, shows a striking
257 correspondence with the Macusani matrix glasses and a rather similar pattern with the Morococala
258 glass inclusions. The major discrepancy is shown by Li, which is very low in the East Pisco Basin

tephra (Table 6, Fig. 6e). Lithium, however, is a highly mobile element and volcanic glass may be depleted in Li during post-depositional processes, as recently reported in several studies (e.g., Misra and Froelich 2012; Hofstra et al. 2013; Ellis et al. 2018).

The age of the MH-T4 tephra eruption was determined on biotite and muscovite due to the fact that the consistent mineral assemblage and composition indicate that the ash layer represents deposition from a single eruption, with both muscovite and biotite as juvenile phenocrysts. The quantitative compositional data indicate that submarine alteration was not pervasive, allowing us to determine the age of the eruption. The ^{39}Ar–^{40}Ar ages determined separately on the two micas are identical, 7.95 ± 0.03 Ma and 7.98 ± 0.03 Ma, and allow us to propose a weighted average age of 7.96 ± 0.02 Ma for this eruption. This age is more reliable and precise than the previous age of 8.05 ± 0.14 Ma obtained from biotite by Bosio et al. (2020b); biotite shows a lower Ca concentration than the previous sample, which indicates a reduced amount of Ca-rich impurities/alteration phases (Fig. 7b).

The age of 7.96 ± 0.02 Ma falls within the literature age range of the Peruvian Macusani volcanics, between ca. 10 and 4 Ma (Pichavant et al. 1988a; Cheilletz et al. 1992; Poupeau et al. 1993) and with the late Miocene ages of the Bolivian Morococala volcanic field (Koeppen et al. 1987; Morgan et al. 1998). According to Cheilletz et al. (1992), the Macusani eruption ages (i.e. 10.0 ± 0.5 Ma, 7.8-8.0 ± 0.1 Ma, 7.5 ± 0.1 Ma, 7.3 ± 0.1 Ma, 6.8-7.0 ± 0.1 Ma, 6.7 ± 0.1 Ma) cluster in correspondence to two important Andean tectonic phases, with the second cluster being by far the most voluminous. These ages are in agreement with the K-Ar ages reported by Pichavant et al. (1988a), i.e. 10.5 ± 0.5 Ma, 7.6 ± 0.3 Ma, 7.1 ± 0.7 Ma and 6.8 ± 0.2 Ma, and with those proposed by Poupeau et al. (1993), i.e. 7 ± 1 Ma and late episodes at 5.7–5.3 and 4.8–4.3 Ma. The late Miocene ages of 7.6–8 Ma for Macusani agree with the 7.96 Ma age of the two-mica tephra. MH-T4 age also overlaps with the Morococala late Miocene ages. According to ^{39}Ar–^{40}Ar dating, the andalusite-bearing rhyolites give an age of ca. 8.4 Ma, the cordierite-bearing rhyolites 6.8 Ma, and the quartz latites 6.4 Ma (Koeppen et al. 1987). Since the two-mica volcanic products are only

present in the andalusite-bearing rhyolites, only the age of this unit should be taken into account for comparison with the Pisco tephra. This age is consistent with the 7.96 ± 0.02 Ma age of MH-T4.

The CLQ-T23/LB-T19 tephra can be traced and recognized by tephra fingerprinting and correlation for over 6 km at both the localities of Cerro los Quesos (CLQ-T23) and Cerro la Bruja (LB-T19) (Bosio et al., 2019). The age, indirectly bracketed by ^{39}Ar–^{40}Ar dating of ash layers in the same stratigraphic sections (Di Celma et al. 2017; Gariboldi et al. 2017), is between 7.45 ± 0.01 Ma and 6.93 ± 0.09 Ma. Direct age determination could not be achieved here because of the small size of biotite phenocrysts. This late Miocene age overlaps with the late Miocene eruptions of both the Macusani and Morococala volcanic fields (Cheilletz et al. 1992; Koeppen et al. 1987).

The characteristics of the MH-T4 and CLQ-T23/LB-T19 tephra, such as the grain-size classification as extremely fine ash following White and Houghton (2006), correspond to deposition of distal ash from fallout from Plinian plume-cloud systems or co-ignimbrite plumes rising above pyroclastic density currents. The good correspondence of the mineral assemblage, composition of mineral and glass phases, and the smaller distance from vents suggest to propose a correlation of MH-T4 tephra with the Macusani field ignimbrites. We suggest that a major eruption of the Macusani field occurred at 7.96 Ma and that the MH-T4 layer could correspond to one of the largest events of the Macusani region, with ash deposited at over 500 km of distance.

These results indicate that the coastal basins of Peru are highly promising as archives for distal ash from Central Andes eruptions and supereruptions, not only from the Western Cordillera and Altiplano but also from the Eastern Cordillera. Future studies may lead to a better reconstruction of the volcanic history of the Central Andes of Southern Peru.

Conclusion

Few strongly peraluminous volcanic eruptions are reported in the Central Andes and, among these, two-mica volcanics are particularly rare. The mineral assemblage and the mineral and glass composition of the two-mica Pisco ash correspond to the Macusani volcanic complex, active

311 between 10 and 4 Ma in the Eastern Cordillera of Peru, and to the late Miocene Morococala, in
312 northern Bolivia. Concordant biotite and muscovite age determinations indicate an age of 7.96 Ma ±
313 0.02 Ma. This age, together with the petrographic correspondence and the smaller distance between
314 source and sample, lead us to suggest a correlation with the Macusani volcanic field. These results
315 provide new data on the volcanic activity of the Central Andes, suggesting that a major explosive
316 eruption at 7.96 Ma, probably from the Macusani field. This resulted in the dispersal of co-
317 ignimbrite ash to over 500 km to the west, and into the forearc marine basins. This finding possibly
318 represents the farthest occurrence of Eastern Cordillera volcanics in the geological record, and
319 highlights the importance of the exhumed forearc basins as an archive of distal ash from Central
320 Andes volcanoes.
321
322 **Acknowledgements**
323 The authors are grateful to R. Varas-Malca and W. Aguirre for their assistance in the field and at the
324 Natural History Museum in Lima. Special thanks to E. Malinverno for the support in the field and
325 in laboratory analyses, to V. Barberini for the help in ^{39}Ar–^{40}Ar dating, and N. Fusi for grain-size
326 analyses. The authors wish to thank A. Risplendente for the help with the microprobe analyses.
327 Finally, the authors would like to thank an anonymous reviewer, the Executive Editor and the
328 handling Editor V.S. Kamenetsky for the revision and support during publication.
329
330 **Funding**
331 This study was supported by grants from the Italian Ministero dell'Istruzione dell'Università e della
332 Ricerca (PRIN Project 2012YJSBMK) and by the University of Pisa PRA_2015_0028 and
333 PRA_2017_0032 grants.
334
335 **References**

336 Abdel-Rahman A.M. (1994) Nature of biotites from alkaline, calc-alkaline, and peraluminous
337 magmas. J Petrol 35:525-54.

338 Baker MCW, Francis PW (1978) Upper Cenozoic volcanism in the Central Andes—ages and
339 volumes. Earth Planet Sci Lett 41(2):175-187.

340 Blott SJ, Pye K (2001) Gradistat: a grain size distribution and statistics package for the analysis of
341 unconsolidated sediments. Earth Surf Proc Land 26:1237-1248.

342 Barnes VE, Edwards G, McLaughlin WA, Friedman I, Joensuu O (1970) Macusanite Occurrence,
343 Age, and Composition, Macusani, Peru. Geol Soc Am Bull 81:1539-1546.

344 Bianucci G, Di Celma C, Collareta A, Landini W, Post K, Tinelli C, de Muizon C, Bosio G,
345 Gariboldi K, Gioncada A, Malinverno E, Cantalamessa G, Altamirano-Sierra A, Salas-Gismondi R,
346 Urbina M, Lambert O (2016a) Fossil marine vertebrates of Cerro Los Quesos: distribution of
347 cetaceans, seals, crocodiles, seabirds, sharks, and bony fish in a late Miocene locality of the Pisco
348 Basin, Peru. J Maps 12:1037-1046.

349 Bianucci G, Di Celma C, Landini W, Post K, Tinelli C, de Muizon C, Gariboldi K, Malinverno E,
350 Cantalamessa G, Gioncada A, Collareta A, Salas-Gismondi R, Varas-Malca RM, Urbina M,
351 Lambert O (2016b) Distribution of fossil marine vertebrates in Cerro Colorado, the type locality of
352 the giant raptorial sperm whale Livyatan melvillei (Miocene, Pisco Formation, Peru). J Maps 12:
353 543-557.

354 Bianucci G, Bosio G, Malinverno E, de Muizon C, Villa IM, Urbina M, Lambert O (2018). A new
355 large squalodelphinid (Cetacea, Odontoceti) from Peru sheds light on the Early Miocene
356 platanistoid disparity and ecology. Roy Soc Open Sci 5:172302.

357 Bosio G, Gioncada A, Malinverno E, Di Celma C, Villa IM, Cataldi G, Gariboldi K, Collareta A,
358 Urbina M, Bianucci G (2019) Chemical and petrographic fingerprinting of volcanic ashes as a tool

for high-resolution stratigraphy of the upper Miocene Pisco Formation (Peru). J Geol Soc London 176:13-28.

Bosio G, Malinverno E, Collareta A, Di Celma C, Gioncada A, Parente M, Berra F, Marx FG, Vertino A, Urbina M, Bianucci G (2020a) Strontium Isotope Stratigraphy and the thermophilic fossil fauna from the middle Miocene of the East Pisco Basin (Peru). J S Am Earth Sci, 97:102399.

Bosio G, Malinverno E, Villa IM, Di Celma C, Gariboldi K, Gioncada A, Barberini V, Urbina M, Bianucci G (2020b) Tephrochronology and chronostratigraphy of the Miocene Chilcatay and Pisco formations (East Pisco Basin, Peru). Newsl Stratigr 53(2):213-247. DOI: 10.1127/nos/2019/0525

Breitkreuz C, de Silva SL, Wilke HG, Pfander JA, Renno AD (2014) Neogene to Quaternary ash deposits in the Coastal Cordillera in northern Chile: Distal ashes from supereruptions in the Central Andes. J Volcanol Geoth Res 269:68-82.

Caffe PJ, Trumbull RB, Siebel W (2012) Petrology of the Coyaguayma ignimbrite, northern Puna of Argentina: Origin and evolution of a peraluminous high-SiO2 rhyolite magma. Lithos 134-135:179-200.

Cheilletz A, Clark AH, Farrar E, Arroyo Pauca G, Pichavant M, Sandeman HA (1992) Volcano-stratigraphy and 40Ar/39Ar geochronology of the Macusani ignimbrite field: monitor of the Miocene geodynamic evolution of the Andes of southeast Peru. Tectonophysics 205:307-327.

Clarke, DB (1981) The mineralogy of peraluminous granites; a review. The Canadian Mineralogist 19:3-17.de Silva SL, Francis PW (1991) Volcanoes of the Central Andes. Springer-Verlag, New York.

Di Celma C, Malinverno E, Bosio G, Collareta A, Gariboldi K, Gioncada A, Molli G, Basso D, Varas-Malca R, Pierantoni PP, Villa IM, Lambert O, Landini W, Sarti G, Cantalamessa G, Urbina M, Bianucci G (2017) Sequence stratigraphy and palaeontology of the upper Miocene Pisco

382 Formation along the western side of the lower Ica valley (Ica desert, Peru). Riv Ital Paleontol S
383 123:255-274.

384 Di Celma C, Malinverno E, Bosio G, Gariboldi K, Collareta A, Gioncada A, Landini W, Pierantoni
385 PP, Bianucci G (2018) Intraformational unconformities as a record of Late Miocene eustatic falls of
386 sea level in the Pisco Formation (southern Peru). J Maps 14(2):607-619.

387 Dunbar RB, Marty RC, Baker PA (1990) Cenozoic marine sedimentation in the Sechura and Pisco
388 basins, Peru. Palaeogeogr Palaeocl 77:235-261.

389 Ellis, BS, Szymanowski, D, Magna, T, Neukampf, J, Dohmen, R, Bachmann, O, Ulmer, P,
390 Guillong, M (2018) Post-eruptive mobility of lithium in volcanic rocks. Nature communications
391 9:1-9.

392 Esperante R, Brand LR, Chadwick AV, Poma O (2015) Taphonomy and paleoenvironmental
393 conditions of deposition of fossil whales in the diatomaceous sediments of the Miocene/Pliocene
394 Pisco Formation, southern Peru – a new fossil-lagerstätte. Palaeogeogr Palaeocl 417:337-370.

395 Gariboldi K, Bosio G, Malinverno E, Gioncada A, Di Celma C, Villa IM, Urbina M, Bianucci G
396 (2017) Biostratigraphy, geochronology and sedimentation rates of the upper Miocene Pisco
397 Formation at two important marine vertebrate fossil-bearing sites of southern Peru. Newsl Stratigr
398 50(4):417-444.

399 Griffin WL (2008) GLITTER: data reduction software for laser ablation ICP-MS. In Sylvester P
400 (Ed.), Laser Ablation ICP-MS in the Earth Sciences: Current practices and outstanding issues.
401 Mineralogical Association of Canada, Vancouver BC, 308-311.

402 Griggs AJ, Davies SM, Abbott PM, Rasmussen TL, Palmer AP (2014) Optimising the use of
403 marine tephrochronology in the North Atlantic: a detailed investigation of the Faroe Marine Ash
404 Zones II, III and IV. Quaternary Sci Rev 106:122-139.

405 Hart D, Miller DJ (2006) Analysis and correlation of volcanic ash in marine sediments from the
406 Peru margin, Ocean Drilling Program Leg 201: explosive volcanic cycles of the north–central
407 Andes. In: Jørgensen BB, D'Hondt SL & Miller DJ (Eds.) Proceedings of the Ocean Drilling
408 Program, Scientific Results, 201. ODP, College Station, TX, 1-43.

409 Hofstra AH, Todorov TI, Mercer CN, Adams DT, Marsh EE (2013) Silicate Melt Inclusion
410 Evidence for Extreme Pre-eruptive Enrichment and Post-eruptive Depletion of Lithium in Silicic
411 Volcanic Rocks of the Western United States: Implications for the Origin of Lithium-Rich Brines
412 Econ Geol 108:1691-1701

413 Kay SM, Coira BL, Caffe PJ, Chen C-H (2010) Regional chemical diversity, crustal and mantle
414 sources and evolution of central Andean Puna plateau ignimbrites. J Volcanol Geoth Res 198:81-
415 111.

416 Koeppen RP, Smith RL, Kunk MJ, Flores AM, Luedke RG, Sutter JF (1987) The Morococala
417 volcanics: highly peraluminous rhyolite ash flow magmatism in the Cordillera Oriental, Bolivia.
418 Geol Soc Am Abstracts with Programs 19:731.

419 Lebti PP, Thouret J-C, Worner G, Fornari M (2006) Neogene and Quaternary ignimbrites in the
420 area of Arequipa, Southern Peru: Stratigraphical and petrological correlations. J Volcanol Geoth
421 Res 154:251-275.

422 London D, Hervig RL, Morgan GB VI (1988) Melt-vapor solubilities and elemental partitioning in
423 peraluminous granite-pegmatite systems: experimental results with Macusani glass at 200 MPa.
424 Contrib Mineral Petrol 99:360-373.

425 Mamani M, Wörner G, Sempere T (2010) Geochemical variations in igneous rocks of the Central
426 Andean orocline (13°S to 18°S): Tracing crustal thickening and magma generation through time
427 and space. Geol Soc Am Bull 122:162-182.

428 Miller CF (1985) Are strongly peraluminous magmas derived from pelitic sedimentary sources? J
429 Geol 93:673-689.

430 Misra, S, Froelich, PN (2012) Lithium isotope history of Cenozoic seawater: changes in silicate
431 weathering and reverse weathering. Science 335(6070):818-823.

432 Mlynarczyk MSJ, Williams-Jones AE (2005) The role of collisional tectonics in the metallogeny of
433 the Central Andean tin belt. Earth Planet Sc Lett 240:656-667.

434 Morgan GB VI, London D, Luedke RG (1998) Petrochemistry of late-Miocene peraluminous silicic
435 volcanic rocks from the Morococala field, Bolivia. J Petrol 39:601-632.

436 Noble DC, Vogel TA, Peterson PS, Landis GP, Grant NK, Jezek PA, Mc Kee EH (1984) Rare-
437 element enriched, S-type ash-flow tuffs containing phenocrysts of muscovite, andalusite and
438 sillimanite, southeastern Peru. Geology 12:35-39.

439 Peccerillo, A, Taylor, SR (1976) Geochemistry of Eocene calc-alkaline volcanic rocks from the
440 Kastamonu area, northern Turkey. Contrib mineral petr 58:63-81.

441 Pichavant M, Herrera JV, Boulmier S, Briqueu L, Joron J-L, Juteau M, Marin L, Michard A,
442 Sheppard SMF, Treuil M, Vernet M (1987) The Macusani glasses, SE Peru: evidence of chemical
443 fractionation in peraluminous magmas. The Geochemical Soc Special Publication 1:359-373.

444 Pichavant M, Kontak DJ, Valencia Herrera J, Clark AH (1988a) The Miocene–Pliocene Macusani
445 volcanics, SE Peru: I. Mineralogy and magmatic evolution of a two-mica aluminosilicate bearing
446 ignimbrite suite. Contrib Mineral Petr 100:300-324.

447 Pichavant M, Kontak DJ, Briqueu L, Valencia Herrera J, Johnston RM (1988b) The Miocene–
448 Pliocene Macusani Volcanics, SE Peru: II. Geochemistry and origin of a felsic peraluminous
449 magma. Contrib Mineral Petr 100:325-338.

450 Pouclet A, Cambray H, Cadet J-P, Bourgois J, De Wever P (1990) Volcanic ash from leg 112 off
451 Peru. In: Suess E, von Huene R, et al., Proceedings of the ODP, Scientific Results, 112:465-480.

452 Poupeau G, Labrin E, Sabil N, Bigazzi G, Arroyo G, Vatin-Pérignon N (1993) Fission-track dating
453 of 15 macusanite glass pebbles from the Macusani volcanic field (SE Peru). Nucl Tracks Rad Meas,
454 21(4):499–506.

455 Rosenbaum G, Giles D, Saxon M, Betts PG, Weinberg RF, Duboz C (2005) Subduction of the
456 Nazca Ridge and the Inca Plateau: Insights into the formation of ore deposits in Peru. Earth Planet
457 Sc Lett 239:18-32.

458 Sandeman HA, Clark AH, Farrar E (1997) Lithostratigraphy, petrology and 40Ar-39Ar
459 geochronology of the Crucero Supergroup, Puno Department, SE Peru. J S Am Earth Sci 10:223-
460 245.

461 Sandeman HA, Clark AH (2003) Glass-rich, cordierite–biotite rhyodacite, Valle Ninahuisa, Puno,
462 southeastern Peru: petrological evidence for hybridization of "Lachlan S-type" and potassic mafic
463 magmas. J Petrol 44:355-385.

464 Sandeman HA, Clark AH (2004) Commingling and mixing of S-type peraluminous, ultrapotassic
465 and basalticmagmas in the Cayconi volcanic field, Cordillera de Carabaya, SE Peru. Lithos 73:186-
466 213.

467 Schneider A (1987) Eruptive processes, mineralization and isotopic evolution of the Los Frailes,
468 Kari Kari Region, Bolivia. Rev Geol Chile 30:27-33.

469 Shand, SJ (1943) The eruptive rocks. John Wiley & Sons, 2nd edition, New York.

470 Shane P, Smith V, Nairn I (2003) Biotite composition as a tool for the identification of Quaternary
471 tephra beds. Quaternary Res 59:262-270.

472 Tada R, Murray RW et al. (2015) Methods. In: Tada R, Murray RW et al. (eds) Proceedings of the
473 IODP, Expedition Reports, College Station, Texas, 346:1-58.

474 Taylor, SR, McLennan, SM (1985) The continental crust: its composition and evolution. Blackwell
475 Science Inc, United States.

476 Thornburg TM, Kulm LD (1981) Sedimentary basins of the Peru continental margin: Structure,
477 stratigraphy, and Cenozoic tectonics from 6°S to 16°S latitude. In Kulm LD, Dymond J, Dasch EJ,
478 Hussong DM (Eds.), Nazca plate: Crustal formation and Andean convergence 393-422. Boulder,
479 CO: Geol Soc Am Mem 154.

480 Travis RB, Gonzales G, Pardo A (1976) Hydrocarbon potential of coastal basins of Peru. Am Assoc
481 Petr Geol Memoir 25:331-338.

482 Trumbull RB, Riller U, Oncken O, Scheuber E, Munier K, Hongn F (2006) The Time-Space
483 Distribution of Cenozoic Volcanism in the South-Central Andes: a New Data Compilation and
484 Some Tectonic Implications. In: Oncken O et al. (eds) The Andes. Frontiers in Earth Sciences.
485 Springer, Berlin, Heidelberg.

486 Villa IM, Ruggieri G, Puxeddu M, Bertini G (2006) Geochronology and isotope transport
487 systematics in a subsurface granite from the Larderello–Travale geothermal system (Italy). J
488 Volcanol Geoth Res 152:20-50.

489 White JDL, Houghton BF (2006) Primary volcaniclastic rocks. Geology 34:677-680.
490

491 **Figure captions**

492 **Fig. 1** Geographical setting and Eastern Cordillera volcanism of the Central Andes. The orange star
493 shows the East Pisco Basin (EPB) location. Blue stars show the main Eastern Cordillera volcanic
494 fields (MAC = Macusani; MOR = Morococala). CC stays for Coastal Cordillera, PC for Pre-
495 Cordillera, WC for Western Cordillera, A for Altipiano, EC for Eastern Cordillera, SA for
496 Subandean zone

Fig. 2 Geological map of the study area. Geological map of the studied localities in the western side of the Ica River and geographic position of SP tephra mentioned in this paper (red stars) modified from Di Celma et al. (2018) and Bosio et al. (2020b)

Fig. 3 Field photo of Cerros la Mama y la Hija. PE0.2 unconformity (i.e., the unconformity found at the base of the P2 allomember) (red continuous line) and MH-T4 tephra layer (yellow dashed line) at the locality of Cerros la Mama y la Hija

Fig. 4 BSE images and grain-size distribution of peraluminous tephra. **a.** BSE image of 250–500 μm fraction of MH-T4 tephra. **b.** Contours of the crystals shown in Figure 4a showing biotite (bt), plagioclase (pl), K-feldspar (kfs) and muscovite (ms) phenocrysts, and glass shards (gls). **c.** BSE image of a well-preserved muscovite phenocryst surrounded by volcanic glass in the MH-T4 sample. **d.** BSE image of an Al_2SiO_5 mineral inclusion in a high-vesiculated glass shard in the MH-T4 sample. **e.** Grain-size distribution curves of MH-T4 ash layer and the tephra pairs CLQ-T23 and LB-T19. Distribution is unimodal, particle diameter is extremely fine ash. Particle size is shown as both micrometers and ϕ

Fig. 5 Biotite compositional diagrams. **a.** Classification of MH-T4 and CLQ-T23/LB-T19 biotite in the Al^{IV} vs Fe/Fe+Mg diagram of Clarke (1981). For MH-T4, open symbols represent analyses at the Institut des Sciences de la Terre d'Orleans (Orléans, France), and close symbols represent analyses at the Università di Milano (Dipartimento di Scienze della Terra "Ardito Desio", Milano, Italy). Comparison with biotite composition from tephra of the P2 allomember (gray field) and from SP Macusani and Morococala volcanic fields. **b.** MH-T4 and CLQ-T23/LB-T19 biotite in the Ti (apfu) vs Fe/Fe+Mg diagram. Symbols and field as in 5a. **c.** Composition of MH-T4 and CLQ-T23/LB-T19 biotite in Al_2O_3 vs FeO^T diagram according to Abdel-Rahman (1994). Symbols and field as in (a). **d.** Composition of MH-T4 and CLQ-T23/LB-T19 biotite in MgO vs FeO^T diagram according to Abdel-Rahman (1994). Symbols and field as in (a). **e.** Chemical ternary diagram of feldspar phenocrysts from the MH-T4 tephra. Comparison with the SP Macusani feldspar fields

Fig. 6 Composition of matrix glass. **a.** Harker K_2O vs SiO_2 diagram of glass shards showing the glass composition of MH-T4 and CLQ-T23/LB-T19 tephra. Comparison with glass composition from tephra of the P2 allomember (gray field) and from SP Macusani and Morococala volcanic fields. Fields from Peccerillo and Taylor (1976). **b.** CaO vs SiO_2 diagram of glass shards showing the glass composition of MH-T4 and CLQ-T23/LB-T19 tephra. Comparison with glass composition from tephra of the P2 allomember (gray field) and from SP Macusani and Morococala volcanic fields. **c.** Al_2O_3 vs SiO_2 diagram of glass shards showing the glass composition of MH-T4 and CLQ-T23/LB-T19 tephra. Comparison with glass composition from tephra of the P2 allomember (gray field) and from SP Macusani and Morococala volcanic fields. **d.** A/NK vs A/CNK diagram following Shand (1943) of glass shards showing the glass composition of MH-T4 and CLQ-T23/LB-T19 tephra. Comparison with glass composition from SP Macusani and Morococala volcanic fields. **e.** Trace element LA-ICP-MS analysis of matrix glasses for MH-T4 (this work), matrix glasses for Macusani (M. Pichavant, unpublished data) and glass inclusions in quartz for Morococala (Morgan et al. 1998). Values are normalized to Upper Continental Crust (normalizing values from Taylor and McLennan 1985)

Fig. 7 Age spectra, Ca/K vs age and Cl/K vs age diagrams. **a.** MH-T4 age spectra of biotite (red) and muscovite (blue) separates. Uncertainties are shown as 2σ. The isochemical ages (i.e. weighted average age of isochemical steps) are 7.98 ± 0.03 Ma for biotite and 7.95 ± 0.03 Ma for muscovite. **b.** MH-T4 Ca/K vs age diagram of biotite (red full circles), previous dated biotite (red empty circles) and muscovite (blue diamonds) separates. The dashed ellipse includes the lowest Ca/K steps considered for the age calculation. Uncertainties are smaller than symbols. **c.** MH-T4 Cl/K vs age diagram of biotite (red full circles) and previous dated biotite (red empty circles) with a close-up on the muscovite (blue diamonds) points. The dashed ellipse includes the lowest Cl/K steps considered for the age calculation. Uncertainties are smaller than symbols

Tables

548 **Table 1a** EPMA analyses on biotite phenocrysts of MH-T4 tephra. The first number is the crystal
549 and the second one represents the core (1) or the rim (2). Comparison with the Macusani and
550 Morococala mean biotite compositions from literature. **"**AR" is the abbreviation for andalusite-
551 bearing rhyolites in Morgan et al. (1998). X is K+Na+Ba and Y is AlVI+Mg+
552 Fe+Mn+Ti. Abbreviations "na" stay for "not analyzed" and "bd" stay for "below detection"
553 **Table 1b** EPMA analyses on biotite phenocrysts of MH-T4 tephra (continuation). The first number
554 is the crystal and the second one represents the core (1) or the rim (2). Comparison with the
555 Macusani and Morococala mean biotite compositions from literature. **"**AR" is the abbreviation for
556 andalusite-bearing rhyolites in Morgan et al. (1998). X is K+Na+Ba and Y is AlVI+Mg+
557 Fe+Mn+Ti. Abbreviations "na" stay for "not analyzed" and "bd" stay for "below detection"
558 **Table 2** EPMA analyses on muscovite phenocrysts of MH-T4 tephra. Comparison with the
559 Macusani and Morococala mean muscovite compositions from literature. **"**AR" is the abbreviation
560 for andalusite-bearing rhyolites in Morgan et al. (1998). Abbreviations "na" stay for "not analyzed"
561 and "bd" stay for "below detection"
562 **Table 3** EPMA analyses on feldspar phenocrysts of MH-T4 tephra. Plagioclase and sanidine
563 phenocrysts are compared with the Macusani and Morococala mean compositions from literature.
564 **"**AR" is the abbreviation for andalusite-bearing rhyolites in Morgan et al. (1998). Abbreviations
565 "na" stay for "not analyzed" and "bd" stay for "below detection"
566 **Table 4** EPMA analyses on Al_2SiO_5 minerals of MH-T4 tephra. Comparison with the Macusani and
567 Morococala mean compositions of sillimanite and andalusite from literature. **"**AR" is the
568 abbreviation for andalusite-bearing rhyolites in Morgan et al. (1998). Abbreviations "na" stay for
569 "not analyzed" and "bd" stay for "below detection"
570 **Table 5** EPMA analyses on distal ash glass shards of MH-T4 tephra reported as means and standard
571 deviations. Comparison with the Macusani and Morococala matrix glass analyses from literature.
572 "CR" is the abbreviation for cordierite-bearing rhyolites in Morgan et al. (1998). Concentrations are
573 normalized to 100 and the original EPMA total of MH-T4 is shown

574 **Table 6** Trace element LA-ICP-MS analysis of matrix glasses for MH-T4 tephra

575 **Table 7** ^{39}Ar–^{40}Ar dating results of MH-T4 biotite phenocrysts. Analytical data show step number,
576 step temperature, ^{40}Ar total, ^{40}Ar uncertainty, radiogenic ^{40}Ar, ^{39}Ar, ^{39}Ar uncertainty, ^{39}Ar
577 percentage, ^{38}Ar, ^{38}Ar uncertainty, $^{38}ArCl$, ^{37}Ar, ^{37}Ar uncertainty, ^{36}Ar, ^{36}Ar uncertainty, step age,
578 age uncertainty as 1σ, Ca/K ratio and its uncertainty, Cl/K ratio and its uncertainty, $^{39}Ar/^{40}Ar$,
579 $^{39}Ar/^{40}Ar$ uncertainty, $^{36}Ar/^{40}Ar$, $^{36}Ar/^{40}Ar$ uncertainty

580 **Table 8** ^{39}Ar–^{40}Ar dating results of MH-T4 muscovite phenocrysts. Analytical data show step
581 number, step temperature, ^{40}Ar total, ^{40}Ar uncertainty, radiogenic ^{40}Ar, ^{39}Ar, ^{39}Ar uncertainty, ^{39}Ar
582 percentage, ^{38}Ar, ^{38}Ar uncertainty, $^{38}ArCl$, ^{37}Ar, ^{37}Ar uncertainty, ^{36}Ar, ^{36}Ar uncertainty, step age,
583 age uncertainty as 1σ, Ca/K ratio and its uncertainty, Cl/K ratio and its uncertainty, $^{39}Ar/^{40}Ar$,
584 $^{39}Ar/^{40}Ar$ uncertainty, $^{36}Ar/^{40}Ar$, $^{36}Ar/^{40}Ar$ uncertainty

585

Figure 1 - 1 column width

Click here to access/download;Figure;BV_Figure 1.tif

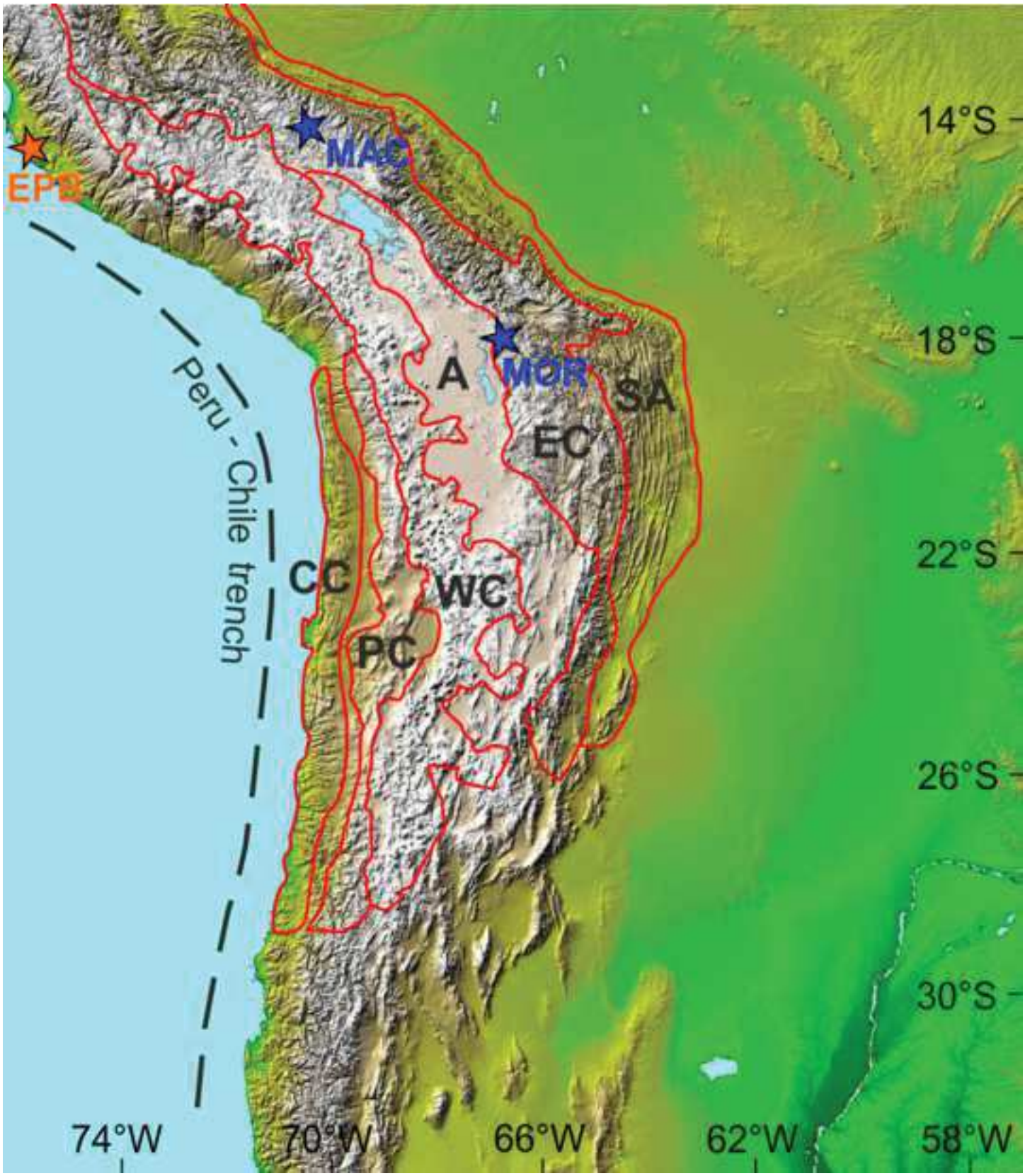

Your image file "BV_Figure 2_rev.tif" cannot be opened and processed.
Please see the common list of problems, and suggested resolutions below.

Reason: The image file is corrupt or invalid. Please check and resubmit.

Other Common Problems When Creating a PDF from an image file

You will need to convert your image file to another format or fix the current image, then re-submit it.

Figure 3 - 2 column width

Click here to access/download;Figure;BV_Figure 3_rev.tif

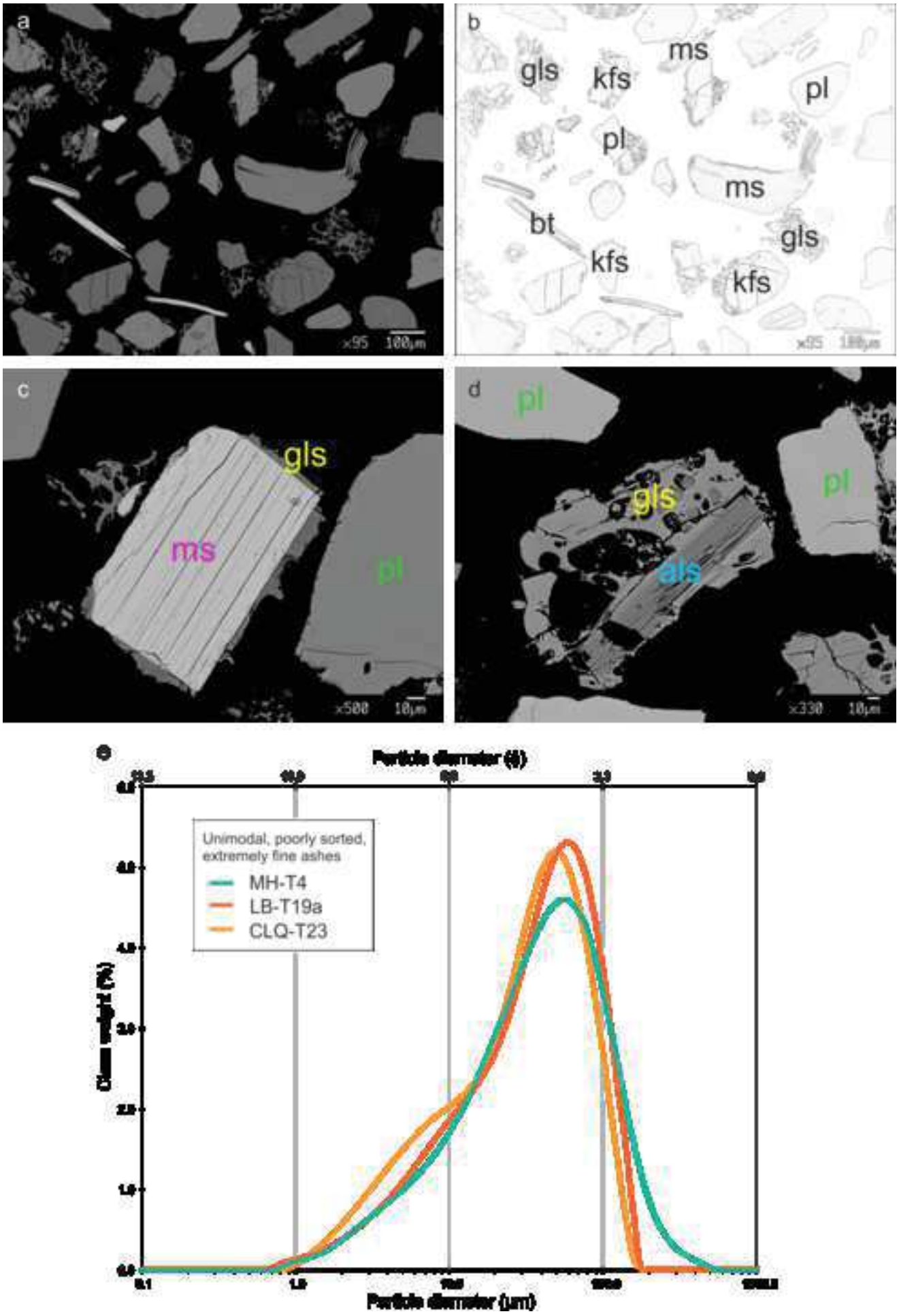

Your image file "BV_Figure 5_rev.tif" cannot be opened and processed.
Please see the common list of problems, and suggested resolutions below.

Reason: The image file is corrupt or invalid. Please check and resubmit.

Other Common Problems When Creating a PDF from an image file

You will need to convert your image file to another format or fix the current image, then re-submit it.

Your image file "BV_Figure 6.tif" cannot be opened and processed. Please see the common list of problems, and suggested resolutions below.

Reason: The image file is corrupt or invalid. Please check and resubmit.

Other Common Problems When Creating a PDF from an image file

You will need to convert your image file to another format or fix the current image, then re-submit it.

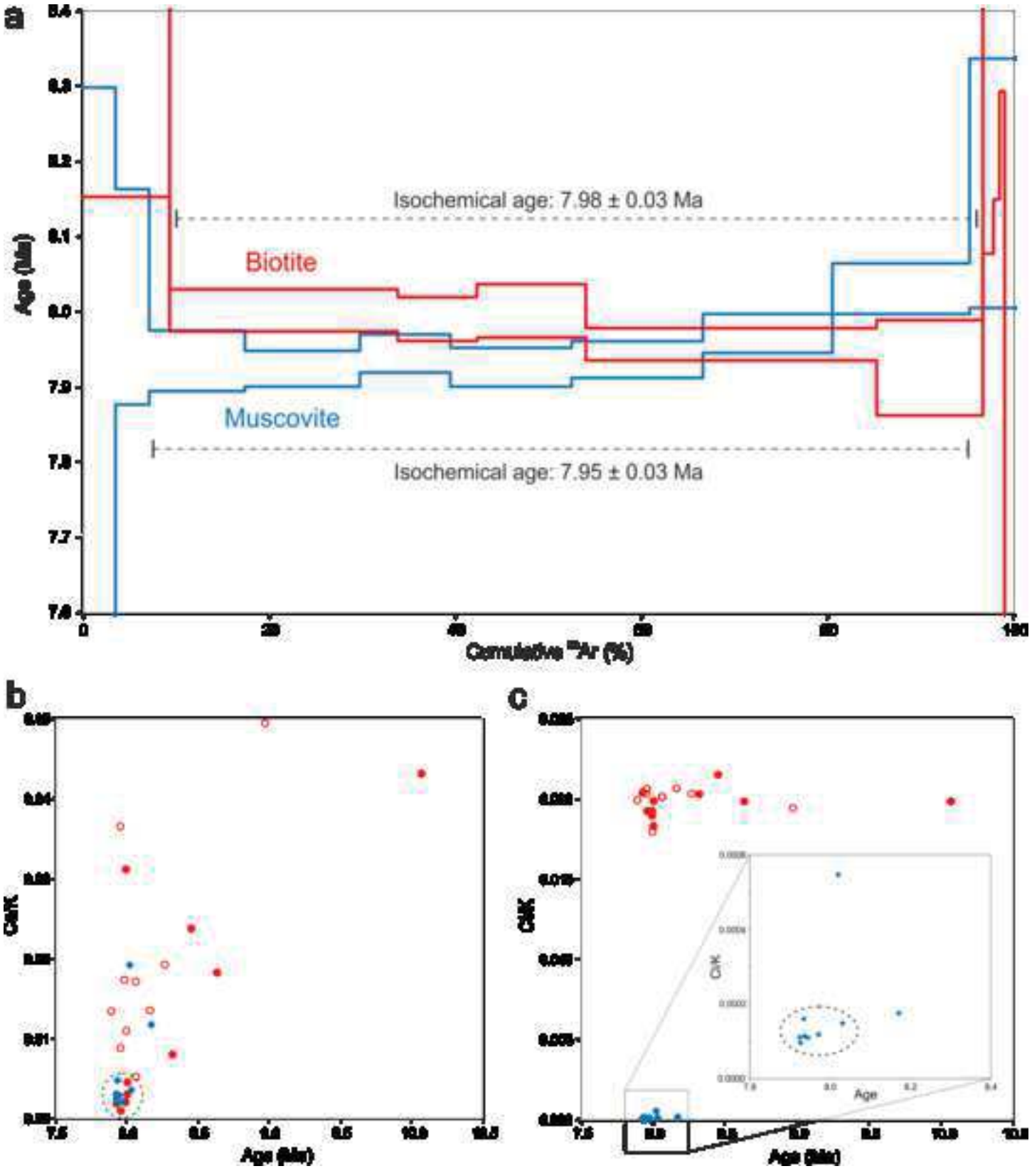

Table 1

Provenance of samples:	MH-T4 - PISCO BASIN																													
Source:	*This work*																													
	1-1	1-2	2-1	2-2	3-1	3-2	4-1	4-2	5-1	5-2	6-1	6-2	7-1	7-2	8-1	8-2	9-1	9-2	10-1	10-2	11-1	11-2	12-1	12-2	13-1	13-2	14-1	14-2	15-1	15-2
SiO_2 wt%	34.83	35.32	35.76	34.94	35.79	35.06	34.73	35.61	35.42	35.15	35.98	34.92	34.96	35.47	35.72	35.53	34.12	34.96	34.91	34.64	34.20	34.62	34.43	34.95	34.93	34.86	34.07	33.85	34.77	34.90
TiO_2	3.69	3.51	2.98	3.17	3.06	3.01	3.85	3.75	3.66	3.76	3.25	3.24	3.31	3.32	3.81	3.72	3.45	3.39	3.75	3.72	3.23	3.28	3.08	2.96	3.62	3.74	3.79	3.67	3.37	3.11
Al_2O_3	19.25	19.33	18.85	18.36	19.67	19.54	18.86	18.90	18.75	18.81	19.23	19.18	19.39	19.60	18.92	18.92	18.54	19.09	18.96	18.79	19.29	19.08	19.96	19.68	18.56	18.77	18.22	18.40	19.19	19.18
FeO^T	20.71	21.23	21.93	22.24	21.16	21.30	20.73	20.85	20.64	20.84	22.17	22.33	20.84	20.76	21.02	20.75	21.80	21.66	21.01	20.68	21.73	21.52	21.15	20.88	20.32	20.20	20.48	20.36	20.70	20.63
MnO	0.17	0.13	0.31	0.28	0.25	0.23	0.10	0.17	0.14	0.13	0.27	0.18	0.17	0.21	0.11	0.11	0.18	0.15	0.07	0.10	0.15	0.17	0.22	0.25	0.15	0.08	0.16	0.10	0.20	0.20
MgO	6.87	6.94	5.56	5.35	6.13	6.34	7.21	7.33	7.18	7.01	5.49	5.65	6.60	6.67	7.16	7.18	6.44	6.21	7.30	7.33	6.20	6.06	6.21	6.10	7.22	7.20	7.23	7.18	6.66	6.66
CaO	bd	bd	0.02	bd	bd	bd	bd	0.04	bd	bd	0.01	bd	0.01	0.01	0.02	0.02	0.01	0.03	0.01	bd	0.03	bd	0.02	0.01	0.04	0.03	0.01	0.03	0.01	0.04
Na_2O	0.38	0.35	0.34	0.37	0.27	0.39	0.35	0.30	0.33	0.26	0.34	0.43	0.37	0.35	0.33	0.32	0.28	0.34	0.33	0.29	0.33	0.29	0.39	0.31	0.36	0.32	0.34	0.33	0.36	0.33
K_2O	9.05	8.88	8.94	8.93	9.14	9.13	9.04	8.98	9.21	9.14	8.94	8.76	9.20	9.08	9.12	9.01	9.11	9.12	9.15	9.12	8.85	8.89	9.06	9.06	9.10	9.15	9.06	9.07	9.04	9.09
F	na	na	na	na	na	na	na	na	na	na	na	na	na	na	na	na	na	na	na	na	na	na	na	na	na	na	na	na	na	na
Cl	0.10	0.09	0.16	0.17	0.05	0.05	0.15	0.14	0.17	0.18	0.18	0.17	0.07	0.06	0.11	0.14	0.10	0.13	0.15	0.14	0.17	0.18	0.05	0.05	0.17	0.17	0.16	0.18	0.09	0.08
ZnO	na	na	na	na	na	na	na	na	na	na	na	na	na	na	na	na	na	na	na	na	na	na	na	na	na	na	na	na	na	na
BaO	0.11	0.20	0.13	0.09	0.09	0.06	0.20	0.09	0.02	0.00	0.06	0.00	0.16	0.14	0.10	0.35	0.09	0.07	0.09	0.13	0.00	0.10	0.02	0.00	0.04	0.13	0.35	0.04	0.17	0.06
Total	95.15	95.98	94.98	93.90	95.61	95.12	95.28	96.25	95.58	95.33	95.93	94.95	95.10	95.67	96.43	96.05	94.12	95.15	95.77	94.98	94.18	94.19	94.64	94.31	94.51	94.65	93.86	93.23	94.55	94.29
Ions on the basis of 22 oxygens																														
Si apfu	5.35	5.38	5.52	5.48	5.46	5.40	5.34	5.40	5.41	5.38	5.49	5.40	5.38	5.41	5.41	5.41	5.34	5.39	5.34	5.34	5.33	5.39	5.33	5.41	5.39	5.37	5.34	5.32	5.38	5.41
Ti	0.43	0.40	0.35	0.37	0.35	0.35	0.44	0.43	0.42	0.43	0.37	0.38	0.38	0.38	0.43	0.43	0.41	0.39	0.43	0.43	0.38	0.38	0.36	0.34	0.42	0.43	0.45	0.43	0.39	0.36
Al	3.49	3.47	3.43	3.39	3.54	3.55	3.42	3.38	3.37	3.40	3.46	3.50	3.52	3.52	3.38	3.39	3.42	3.47	3.42	3.41	3.54	3.50	3.64	3.59	3.38	3.41	3.36	3.41	3.50	3.50
AlIV	2.65	2.62	2.48	2.52	2.54	2.60	2.66	2.60	2.59	2.62	2.51	2.60	2.62	2.59	2.59	2.59	2.66	2.61	2.66	2.66	2.67	2.61	2.67	2.59	2.61	2.63	2.66	2.68	2.62	2.59
AlVI	0.83	0.85	0.95	0.87	1.00	0.94	0.75	0.78	0.78	0.78	0.95	0.90	0.90	0.93	0.78	0.80	0.77	0.86	0.75	0.75	0.87	0.89	0.97	1.00	0.77	0.79	0.70	0.73	0.88	0.91
Fe	2.66	2.70	2.83	2.92	2.70	2.74	2.66	2.64	2.64	2.67	2.83	2.89	2.68	2.65	2.66	2.64	2.86	2.79	2.69	2.67	2.83	2.80	2.74	2.70	2.62	2.60	2.68	2.68	2.68	2.67
Mn	0.02	0.02	0.04	0.04	0.03	0.03	0.01	0.02	0.02	0.02	0.04	0.02	0.02	0.03	0.01	0.01	0.02	0.02	0.01	0.01	0.02	0.02	0.03	0.03	0.02	0.01	0.02	0.01	0.03	0.03
Mg	1.57	1.58	1.28	1.25	1.39	1.45	1.65	1.66	1.63	1.60	1.25	1.30	1.51	1.52	1.62	1.63	1.50	1.43	1.66	1.68	1.44	1.41	1.43	1.41	1.66	1.65	1.69	1.68	1.54	1.54
Ca	bd	bd	bd	bd	bd	bd	bd	0.01	bd	bd	bd	bd	bd	bd	bd	bd	bd	0.01	bd	bd	0.01	bd	bd	bd	0.01	0.01	bd	0.01	bd	0.01
Na	0.11	0.10	0.10	0.11	0.08	0.12	0.11	0.09	0.10	0.08	0.10	0.13	0.11	0.10	0.10	0.10	0.09	0.10	0.10	0.09	0.10	0.09	0.12	0.09	0.11	0.10	0.10	0.10	0.11	0.10
K	1.77	1.73	1.76	1.79	1.78	1.79	1.77	1.74	1.79	1.79	1.74	1.73	1.81	1.77	1.76	1.75	1.82	1.79	1.78	1.79	1.76	1.77	1.79	1.79	1.79	1.80	1.81	1.82	1.78	1.80

Cl	0.02	0.02	0.04	0.05	0.01	0.01	0.04	0.04	0.04	0.05	0.05	0.05	0.02	0.02	0.03	0.04	0.03	0.03	0.04	0.04	0.04	0.05	0.01	0.01	0.04	0.04	0.04	0.05	0.02	0.02
Zn	na	na	na	na	na	na	na	na	na	na	na	na	na	na	na	na	na	na	na	na	na	na	na	na	na	na	na	na	na	na
Ba	0.01	0.01	0.01	0.01	0.01	bd	0.01	0.01	bd	bd	bd	bd	0.01	0.01	0.01	0.02	0.01	bd	0.01	0.01	bd	0.01	bd	bd	bd	0.01	0.02	bd	0.01	bd
sum	15.43	15.41	15.36	15.40	15.35	15.44	15.46	15.40	15.43	15.41	15.33	15.40	15.45	15.39	15.41	15.41	15.50	15.43	15.47	15.47	15.45	15.41	15.45	15.39	15.45	15.44	15.51	15.50	15.44	15.43
X	1.89	1.84	1.87	1.91	1.86	1.91	1.89	1.84	1.89	1.86	1.84	1.86	1.93	1.88	1.86	1.87	1.91	1.90	1.89	1.89	1.86	1.86	1.91	1.88	1.91	1.91	1.93	1.92	1.90	1.90
Y	5.51	5.55	5.44	5.45	5.48	5.52	5.53	5.52	5.49	5.50	5.44	5.49	5.50	5.50	5.51	5.51	5.56	5.49	5.54	5.55	5.54	5.50	5.52	5.49	5.50	5.49	5.54	5.53	5.51	5.51
Mgv	0.37	0.37	0.31	0.30	0.34	0.35	0.38	0.39	0.38	0.37	0.31	0.31	0.36	0.36	0.38	0.38	0.34	0.34	0.38	0.39	0.34	0.33	0.34	0.34	0.39	0.39	0.39	0.39	0.36	0.37

Table 1a

Provenance of samples:	MH-T4 - PISCO BASIN																	MACUSANI VOLCANIC FIELD					MOROCOCALA VOLCANIC FIELD					
Source:	*This work*																	*Noble et al. (1984)*			*Pichavant et al. (1988a)*		*Morgan et al. (1998)*					
	16-1	16-2	17-1	17-2	18-1	18-2	19-1	19-2	20	21	22	23	24	25	26	27	28	mean (6)	mean (6)	mean (10)	mean (15)	SD	AR mean (164)	SD	AR mean (91)	SD	AR mean (113)	SD
SiO_2 wt%	35.06	35.52	34.03	34.23	34.61	34.08	34.73	34.01	35.16	35.19	34.88	34.81	35.22	34.93	35.57	34.35	34.85	36.30	36.40	35.30	36.01	0.71	34.79	0.49	35.24	0.44	34.91	1.02
TiO_2	3.20	3.21	3.51	3.45	3.60	3.80	3.23	3.09	3.36	3.06	3.28	2.94	3.45	3.37	2.94	3.50	3.33	2.55	2.88	2.94	2.76	0.96	2.88	0.26	2.89	0.28	2.91	0.21
Al_2O_3	19.11	18.99	18.00	18.59	18.99	18.52	18.98	18.94	19.85	20.30	20.07	20.11	19.13	19.18	19.91	18.84	19.33	21.10	19.60	21.30	20.29	0.94	20.30	0.76	20.60	0.86	20.12	0.92
FeO	20.33	20.62	20.82	20.55	20.42	20.68	22.13	21.33	22.70	19.43	20.02	21.39	20.59	21.27	21.62	21.04	21.02	21.40	23.00	22.80	21.46	1.48	23.84	0.97	22.25	1.70	23.31	1.66
MnO	0.20	0.16	0.17	0.13	0.14	0.10	0.21	0.22	0.11	0.15	0.23	0.34	0.24	0.17	0.21	0.20	0.19	0.01	0.01	0.02	0.18	0.07	0.30	0.08	0.33	0.13	0.28	0.10
MgO	6.68	6.65	6.62	6.72	7.15	7.19	5.45	5.44	6.03	7.31	7.23	5.28	7.23	6.88	4.98	6.20	6.60	4.71	5.03	4.71	4.96	1.07	4.92	0.89	5.22	1.23	5.12	0.63
CaO	0.01	bd	0.03	0.04	0.01	0.02	bd	0.01	0.01	bd	bd	bd	0.04	0.02	bd	bd	bd	bd	bd	bd	0.06	0.11	bd	bd	bd	bd	bd	bd
Na_2O	0.30	0.30	0.33	0.39	0.33	0.35	0.36	0.42	0.38	0.36	0.31	0.29	0.32	0.31	0.37	0.31	0.30	0.37	0.35	0.36	0.49	0.12	0.40	0.02	0.40	0.03	0.40	0.03
K_2O	9.13	9.11	8.98	9.02	9.07	9.08	8.95	9.00	8.65	8.72	8.80	9.25	9.36	9.08	9.16	9.40	9.43	9.12	8.63	8.84	9.00	0.36	8.73	0.19	8.83	0.20	8.67	0.26
F	na	na	na	na	na	na	na	na	na	na	na	bd	bd	bd	0.08	bd	bd	0.01	0.01	0.02	2.45	0.93	2.54	0.71	3.47	0.71	3.39	0.96
Cl	0.05	0.05	0.10	0.11	0.16	0.15	0.13	0.15	0.14	0.08	0.06	na	na	na	na	na	na	0.10	0.17	0.10	na	na	0.11	0.03	0.12	0.03	0.12	0.03
ZnO	na	na	na	na	na	na	na	na	na	na	na	0.14	bd	0.02	bd	0.18	bd	na	na	na	0.13	0.18	0.15	0.04	0.15	0.04	0.12	0.03

BaO	0.09	bd	0.04	0.10	0.02	0.16	0.09	0.06	bd	bd	bd	na	na	na	na	na	na	na	na	na	0.35	0.11	0.05	0.02	0.05	0.02	0.07	0.06
Total	94.18	94.62	92.68	93.33	94.49	94.13	94.29	92.69	93.69	94.69	95.69	94.81	95.81	95.93	96.74	94.07	95.11	93.69	94.69	95.69	96.14	2.02	97.83	-	98.02	-	97.98	-
Ions on the basis of 22 oxygens																												
Si apfu	5.43	5.47	5.39	5.37	5.35	5.31	5.42	5.39	5.35	5.37	5.33	5.40	5.38	5.36	5.48	5.37	5.37	5.51	5.54	5.36	5.42	0.24	5.58	-	5.87	-	6.09	-
Ti	0.37	0.37	0.42	0.41	0.42	0.45	0.38	0.37	0.38	0.35	0.38	0.34	0.40	0.39	0.34	0.41	0.39	0.29	0.33	0.34	0.31	0.11	0.35	-	0.36	-	0.38	-
Al	3.49	3.45	3.36	3.44	3.46	3.40	3.49	3.54	3.56	3.65	3.62	3.67	3.44	3.47	3.62	3.47	3.51	3.77	3.51	3.81	3.60	0.27	3.84	-	4.04	-	4.14	-
AlIV	2.57	2.53	2.61	2.63	2.65	2.69	2.58	2.61	2.65	2.63	2.67	2.60	2.62	2.64	2.52	2.63	2.63	2.49	2.46	2.64	2.58	-	2.42	-	2.13	-	1.91	-
AlVI	0.92	0.91	0.75	0.81	0.80	0.72	0.91	0.94	0.90	1.02	0.95	1.07	0.82	0.84	1.09	0.84	0.88	1.28	1.05	1.17	1.02	-	1.41	-	1.91	-	2.23	-
Fe	2.63	2.65	2.76	2.70	2.64	2.70	2.89	2.83	2.89	2.48	2.56	2.77	2.63	2.73	2.78	2.75	2.71	2.72	2.93	2.89	2.70	0.15	3.20	-	3.10	-	3.40	-
Mn	0.03	0.02	0.02	0.02	0.02	0.01	0.03	0.03	0.01	0.02	0.03	0.04	0.03	0.02	0.03	0.03	0.02	bd	bd	bd	0.02	0.01	0.04	-	0.05	-	0.04	-
Mg	1.54	1.53	1.56	1.57	1.65	1.67	1.27	1.29	1.37	1.66	1.65	1.22	1.65	1.57	1.14	1.45	1.52	1.06	1.14	1.07	1.11	0.25	1.18	-	1.30	-	1.33	-
Ca	bd	bd	0.01	0.01	bd	bd	bd	bd	bd	bd	bd	bd	0.01	bd	bd	bd	bd	bd	bd	bd	0.01	0.02	bd	-	bd	-	bd	-
Na	0.09	0.09	0.10	0.12	0.10	0.11	0.11	0.13	0.11	0.11	0.09	0.09	0.10	0.09	0.11	0.09	0.09	0.11	0.10	0.11	0.14	0.03	0.12	-	0.13	-	0.14	-
K	1.80	1.79	1.82	1.81	1.79	1.81	1.78	1.82	1.68	1.70	1.72	1.83	1.82	1.78	1.80	1.87	1.85	1.77	1.67	1.71	1.73	0.13	1.79	-	1.88	-	1.93	-
Cl	0.01	0.01	0.03	0.03	0.04	0.04	0.03	0.04	0.04	0.02	0.02	na	na	na	na	na	na	0.03	0.04	0.03	bd	bd	0.03	-	0.03	-	0.04	-
Zn	na	na	na	na	na	na	na	na	na	na	na	0.02	bd	bd	bd	0.02	bd	na	na	na	0.01	0.02	0.02	-	0.02	-	0.01	-
Ba	0.01	bd	bd	0.01	bd	0.01	0.01	bd	bd	bd	bd	bd	bd	bd	0.04	bd	bd	bd	bd	bd	0.01	0.01	bd	-	bd	-	bd	-
sum	15.40	15.38	15.47	15.47	15.45	15.51	15.41	15.45	15.39	15.36	15.39	15.38	15.46	15.44	15.34	15.47	15.46	15.25	15.27	15.31	15.33	0.21	16.12	-	16.76	-	17.50	-
X	1.90	1.88	1.92	1.94	1.89	1.92	1.90	1.95	1.79	1.80	1.81	1.92	1.93	1.87	1.95	1.97	1.94	1.87	1.78	1.82	1.89	0.19	1.91	-	2.00	-	2.07	-
Y	5.49	5.48	5.52	5.50	5.52	5.54	5.47	5.45	5.56	5.53	5.56	5.45	5.52	5.55	5.39	5.48	5.52	5.35	5.44	5.46	5.16	-	6.17	-	6.71	-	7.39	-
Mg_V	0.37	0.36	0.36	0.37	0.38	0.38	0.31	0.31	0.32	0.40	0.39	0.31	0.39	0.37	0.29	0.34	0.36	0.28	0.28	0.27	0.29	0.62	0.27	-	0.29	-	0.28	-

Table 1b

Provenance of samples:	MH-T4 - PISCO BASIN																MACUSANI VOLCANIC FIELD					MOROCOCALA VOLCANIC FIELD					
Source:	*This work*																*Noble et al. (1984)*			*Pichavant et al. (1988a)*		*Morgan et al. (1998)*				
	12	13	14	1	2	3-1	3-2	4	5	6	7	8	9	10	16	17	mean (10)	mean (4)	mean (7)	mean (5)	SD	AR mean (102)	SD	AR mean (62)	SD	AR meam (23)	SD
SiO_2 wt%	48.86	48.00	48.12	45.44	45.61	45.63	46.10	44.96	45.68	45.52	45.44	45.59	45.48	45.54	46.28	45.58	47.00	47.00	47.00	45.54	0.79	46.70	0.25	46.74	0.13	46.40	0.3
TiO_2	0.94	0.94	1.36	1.29	0.94	0.77	1.23	0.88	1.07	0.82	1.20	1.19	1.00	1.07	0.95	1.00	0.69	0.70	0.77	0.49	0.28	0.97	0.24	0.91	0.24	0.91	0.18
Al_2O_3	34.82	36.64	36.97	35.53	35.69	33.93	33.57	34.97	35.54	35.51	34.79	35.20	35.16	34.85	33.12	32.76	34.70	35.40	36.20	34.21	1.22	35.15	0.57	34.49	0.28	34.95	0.22
FeO^T	2.44	1.75	1.32	1.25	1.59	2.30	2.05	1.78	1.44	1.60	1.52	1.47	1.34	1.39	2.30	2.45	2.53	2.22	1.38	2.55	0.68	1.83	0.28	1.90	0.24	1.87	0.22
MnO	bd	bd	0.05	0.03	0.02	0.01	0.01	bd	0.01	bd	0.02	0.04	0.06	0.03	0.05	0.09	bd	bd	bd	0.03	0.03	bd	bd	bd	bd	bd	bd
MgO	1.29	0.78	0.71	0.72	0.70	1.18	1.12	0.76	0.77	0.76	0.93	0.89	0.77	0.80	1.40	1.36	1.06	0.92	0.72	1.05	0.08	0.87	0.07	0.87	0.04	0.83	0.08
CaO	0.01	bd	bd	0.01	bd	bd	0.02	0.02	bd	bd	bd	bd	0.01	0.02	0.03	0.08	bd	bd	bd	bd	bd	bd	bd	bd	bd	bd	bd
Na_2O	0.70	0.78	0.79	0.74	0.69	0.72	0.67	0.66	0.72	0.72	0.67	0.69	0.73	0.66	0.73	0.68	0.71	0.70	0.74	0.65	0.05	0.61	0.03	0.68	0.04	0.65	0.04
K_2O	10.92	11.08	10.64	10.22	9.78	9.80	9.82	9.81	9.81	9.71	9.72	9.75	9.60	9.62	10.53	10.27	10.24	10.28	10.32	10.14	0.15	10.14	0.44	9.75	0.17	9.76	0.30
P_2O_5	0.02	0.04	0.03	na	na	na	na	na	na	na	na	na	na	na	bd	0.01	na	na	na	na	na	na	na	na	na	na	na
F	na	na	na	na	na	na	na	na	na	na	na	na	na	na	1.73	1.57	bd	bd	bd	1.49	0.60	2.19	0.92	3.65	0.41	3.72	0.26
Cl	na	na	na	bd	0.01	bd	bd	0.01	0.01	0.01	bd	bd	bd	bd	na	na	0.01	0.02	0.02	na	na	bd	bd	0.01	0.01	0.02	0.01
ZnO	na	na	na	na	na	na	na	na	na	na	na	na	na	na	bd	0.23	na	na	na	0.08	0.10	bd	bd	bd	bd	bd	bd
BaO	na	na	na	bd	0.06	bd	0.10	bd	bd	0.01	0.05	bd	bd	bd	na	na	na	na	na	na	na	0.09	0.12	0.05	0.02	0.05	0.01
Total	93.61	93.27	94.99	95.22	95.09	94.33	94.69	93.84	95.05	94.66	94.33	94.82	94.15	93.98	97.13	96.07	97.00	97.20	97.10	95.91	1.23	97.67	-	97.51	-	97.59	-

Table 2

Table 3

Provenance of samples:	MH-T4 - PISCO BASIN						MACUSANI VOLCANIC FIELD				MOROCOCALA VOLCANIC FIELD					
Source:	*This work*						*Pichavant et al. (1988a)*				*Morgan et al. (1998)*					
Type:	sanidine			plagioclase			sanidine		plagioclase		plagioclase				sanidine	
	12	13	15	16	19	20	mean (3)	SD	mean (7)	SD	AR mean (282)	SD	AR mean (288)	SD	AR mean (537)	SD
SiO_2 wt%	64.44	59.60	64.36	61.67	63.18	62.55	65.06	0.27	62.34	3.12	62.89	1.46	63.53	1.05	64.50	0.32
Al_2O_3	19.21	18.25	19.21	23.54	22.26	22.63	18.90	0.06	23.56	1.94	23.12	1.03	22.72	0.66	19.33	0.11
FeO^T	0.06	0.03	0.01	0.06	0.08	bd	na	na	na	na	0.02	0.01	0.05	0.03	0.02	0.01
CaO	0.05	0.07	0.10	4.11	2.85	3.29	bd	bd	4.58	2.58	3.58	1.15	3.13	0.81	0.05	0.02
Na_2O	2.67	2.81	2.65	8.51	9.41	9.15	3.40	0.13	8.42	1.40	8.89	0.62	9.14	0.47	3.05	0.23
K_2O	12.03	11.54	11.87	0.68	0.68	0.77	11.60	0.24	0.63	0.23	0.67	0.12	0.71	0.06	12.07	0.28
BaO	0.22	0.38	0.13	bd	bd	0.01	0.07	0.08	na	na	na	na	na	na	0.12	0.06
An	0.26	0.37	0.52	20.23	13.78	15.84	0.00	0.00	22.38	12.90	17.49	5.70	15.26	4.00	0.30	0.10
Ab	25.05	26.71	25.14	75.80	82.33	79.71	30.78	1.29	73.96	11.67	78.61	5.20	80.62	3.80	27.62	2.00
Or	74.69	72.92	74.34	3.97	3.89	4.45	69.22	1.29	3.66	1.31	3.90	0.70	4.12	0.40	71.90	1.90
Total	98.72	92.69	98.36	98.57	98.50	98.46	99.00	0.36	99.54	1.04	99.32	-	99.43	-	99.35	-

Table 3

Table 4

Provenance of samples:	MH-T4 - PISCO BASIN						MACUSANI VOLCANIC FIELD						MOROCOCALA VOLCANIC FIELD			
Source:	*This work*						*Noble et al. (1984)*		*Pichavant et al. (1988a)*				*Morgan et al. (1998)*			
Type:	Al_2SiO_5 mineral						sillimanite	andalusite	sillimanite		andalusite		andalusite		andalusite	
	11	12	14	17	18	21	range	range	mean (2)	SD	mean (3)	SD	AR mean (34)	SD	AR mean (39)	SD
SiO_2 wt%	38.25	36.16	36.20	35.60	36.88	36.07	na	na	36.40	0.37	37.25	0.80	36.84	0.19	36.99	0.07
TiO_2	bd	bd	0.01	0.06	bd	bd	0.01 - 0.11	0.01 - 0.34	0.03	0.04	0.04	0.04	0.10	0.03	bd	bd
Al_2O_3	61.51	63.86	64.37	64.51	62.75	64.36	na	na	63.33	0.27	62.14	0.34	62.02	0.36	62.53	0.04
FeO^T	0.22	0.26	0.08	0.22	0.13	0.18	0.04 - 0.44	0.17 - 0.80	0.18	0.05	0.24	0.05	0.61	0.25	0.29	0.02
MnO	bd	0.03	0.04	0.01	bd	0.04	na	na	0.05	0.07	0.03	0.03	bd	bd	bd	bd
MgO	0.02	bd	bd	bd	0.02	bd	na	na	0.02	0.03	0.04	0.02	0.05	0.03	bd	bd
CaO	bd	0.03	bd	0.02	bd	bd	0.01 - 0.20	bd	0.02	0.03	0.01	0.01	bd	bd	bd	bd
Na_2O	bd	0.03	bd	bd	0.02	bd	na	na	bd	bd	bd	bd	bd	bd	bd	bd
K_2O	bd	0.03	bd	0.01	0.09	bd	na	na	bd	bd	bd	bd	bd	bd	bd	bd
Total	98.73	100.41	100.72	100.42	99.90	100.67	-	-	100.02	0.06	99.75	1.01	99.62	-	99.81	-

Table 4

Table 5

Provenance of samples:	MH-T4 - PISCO BASIN		MACUSANI VOLCANIC FIELD					MOROCOCALA VOLCANIC FIELD				
Source:	*This work*		*London et al. (1988)*	*Pichavant et al. (1987)*				*Morgan et al. (1998)*				
Type:	distal ashes glass shards		homogeneous aphyric obsidian	glass pebbles				CR matrix glass				
	Mean (15)	SD		JV1 Mean (5)	CC2 Mean (2)	CM1 Mean (2)	CM2 Mean (2)	CM2 red zone	14 Mean (136)	23 Mean (55)	24 Mean (30)	25 Mean (17)	28 Mean (13)
SiO_2 wt%	73.28	2.55	72.32	72.26	72.69	72.29	72.31	71.95	73.75	74.08	73.78	74.13	74.11
TiO_2	0.05	0.03	0.02	0.07	bd	0.02	0.04	bd	0.07	0.07	0.07	0.07	0.07
Al_2O_3	14.24	0.50	15.63	15.79	16.00	15.92	15.75	15.62	14.07	14.30	14.01	14.12	14.28
FeO^T	0.68	0.11	0.52	0.54	0.56	0.59	0.47	2.75	0.80	0.81	0.78	0.74	0.68
MnO	0.05	0.03	0.06	0.03	0.03	0.08	0.04	0.12	0.04	0.03	0.03	0.03	0.04
MgO	0.08	0.03	0.02	0.02	0.01	0.02	0.01	0.03	0.08	0.08	0.08	0.08	0.08
CaO	0.44	0.07	0.23	0.19	0.10	0.19	0.15	0.26	0.34	0.40	0.46	0.38	0.39
Na_2O	3.57	0.17	4.10	4.29	4.30	4.32	4.27	3.93	2.96	3.19	3.79	3.09	2.77
K_2O	4.95	0.18	3.53	3.83	3.77	3.74	3.88	3.56	5.19	4.98	4.63	4.92	5.31
P_2O_5	0.27	0.09	0.58	na	na	na	na	na	0.25	0.24	0.30	0.23	0.24
ZnO	0.01	0.01	na	na	na	na	na	na	na	na	na	na	na
F	0.27	0.03	1.30	1.34	1.27	1.35	1.33	1.27	0.36	0.24	0.39	0.26	0.31
Cl	bd	-	0.05	na	na	na	na	na	0.11	0.11	0.11	0.12	0.14
$Na_2O + K_2O$	8.52	0.24	7.63	8.12	8.07	8.06	8.15	7.49	8.15	8.17	8.42	8.01	8.08
A/CNK	1.18	0.02	1.42	1.37	1.41	1.38	1.37	1.45	1.27	1.26	1.16	1.27	1.30
Total	92.76	1.22	99.78	98.35	98.73	98.52	98.25	99.49	97.87	98.41	98.26	98.03	98.26

Table 5

	MH-T4 glass 1	MH-T4 glass 2	MH-T4 glass 3
Li (ppm)	9.04	6.70	<11.62
Be	18.2	26.3	47.5
B	865	873	803
Rb	645	584	558
Sr	15.1	16.2	25.1
Zr	14.65	21.2	15.96
Nb	21.0	21.6	19.24
Sn	55.1	68.8	51.2
Cs	166	167	162
Ba	17.08	26.0	33.5
La	1.24	1.71	2.25
Ta	6.12	6.02	5.96
W	26.2	19.1	22.0
Pb	20.3	25.7	29.1
U	19.3	24.9	23.4

Table 6

×MH-T4 biotite										
Weight = 0.01729 g; J = 0.001008; [K] = 8.53 %; [Ca] = 440 ppm; [Cl] = 1680 ppm; Err. = Error										
Step	1	2	3	4	5	6	7	8	9	10
T (°C)	708	796	840	980	1033	1069	1098	1118	1201	1286
^{40}Ar total	3.15×10^{-8}	1.67×10^{-8}	5.45×10^{-9}	8.52×10^{-9}	1.90×10^{-8}	1.15×10^{-8}	2.80×10^{-9}	2.86×10^{-9}	1.00×10^{-8}	6.07×10^{-9}
Err. ^{40}Ar	7.75×10^{-12}	3.37×10^{-12}	1.31×10^{-12}	1.79×10^{-12}	4.38×10^{-12}	2.93×10^{-12}	7.75×10^{-13}	7.75×10^{-13}	3.00×10^{-12}	1.65×10^{-12}
^{40}Ar×	4.48×10^{-9}	1.12×10^{-8}	3.90×10^{-9}	5.37×10^{-9}	1.43×10^{-8}	5.18×10^{-9}	5.48×10^{-10}	3.18×10^{-10}	3.28×10^{-10}	4.48×10^{-10}
^{39}Ar	9.63×10^{-10}	2.55×10^{-9}	8.85×10^{-10}	1.22×10^{-9}	3.25×10^{-9}	1.19×10^{-9}	1.19×10^{-10}	6.69×10^{-11}	5.92×10^{-11}	1.02×10^{-10}
Err. ^{39}Ar	8.93×10^{-13}	2.00×10^{-12}	8.29×10^{-13}	1.10×10^{-12}	2.51×10^{-12}	1.06×10^{-12}	5.13×10^{-13}	5.41×10^{-13}	4.74×10^{-13}	4.77×10^{-13}
% ^{39}Ar	9.26	24.52	8.51	11.71	31.26	11.41	1.15	0.64	0.57	0.98
^{38}Ar	1.44×10^{-10}	3.17×10^{-10}	1.07×10^{-10}	1.41×10^{-10}	3.91×10^{-10}	1.53×10^{-10}	1.64×10^{-11}	9.81×10^{-12}	1.34×10^{-11}	1.55×10^{-11}
Err. ^{38}Ar	2.25×10^{-13}	5.06×10^{-13}	1.64×10^{-13}	2.21×10^{-13}	6.14×10^{-13}	2.39×10^{-13}	2.93×10^{-14}	2.03×10^{-14}	2.43×10^{-14}	2.84×10^{-14}
^{38}Ar$_{Cl}$	1.16×10^{-10}	2.85×10^{-10}	9.57×10^{-11}	1.25×10^{-10}	3.51×10^{-10}	1.36×10^{-10}	1.36×10^{-11}	7.46×10^{-12}	6.60×10^{-12}	1.08×10^{-11}
^{37}Ar	1.18×10^{-11}	6.00×10^{-12}	9.43×10^{-13}	1.90×10^{-12}	1.66×10^{-12}	1.16×10^{-12}	4.95×10^{-13}	6.30×10^{-13}	1.32×10^{-12}	1.64×10^{-12}
Err. ^{37}Ar	7.96×10^{-14}	7.54×10^{-14}	7.25×10^{-14}	7.29×10^{-14}	7.30×10^{-14}	7.28×10^{-14}	7.24×10^{-14}	7.25×10^{-14}	7.27×10^{-14}	7.27×10^{-14}
^{36}Ar	9.04×10^{-11}	1.84×10^{-11}	5.22×10^{-12}	1.06×10^{-11}	1.59×10^{-11}	2.13×10^{-11}	7.55×10^{-12}	8.51×10^{-12}	3.24×10^{-11}	1.88×10^{-11}
Err. ^{36}Ar	2.64×10^{-13}	5.76×10^{-14}	2.00×10^{-14}	3.58×10^{-14}	5.11×10^{-14}	6.69×10^{-14}	2.54×10^{-14}	2.84×10^{-14}	9.61×10^{-14}	5.75×10^{-14}
Age	8.45	8.00	7.99	8.00	7.96	7.93	8.32	8.63	10.07	7.99
Err. age (1σ)	0.15	0.01	0.01	0.02	0.01	0.03	0.12	0.24	0.89	0.31
Ca/K	0.02379	0.00457	0.00207	0.00302	0.00099	0.00190	0.00804	0.01826	0.04316	0.03119
Err. Ca/K	0.00016	0.00006	0.00016	0.00012	0.00004	0.00012	0.00118	0.00211	0.00241	0.00139
Cl/K	0.02152	0.01989	0.01926	0.01832	0.01924	0.02039	0.02030	0.01985	0.01985	0.01895
Err. Cl/K	0.00002	0.00002	0.00002	0.00002	0.00002	0.00002	0.00013	0.00025	0.00025	0.00014
^{39}Ar/^{40}Ar	0.03060	0.15231	0.16225	0.14283	0.17096	0.10286	0.04261	0.02339	0.00591	0.01678
Err. ^{39}Ar/^{40}Ar	2.94×10^{-5}	2.47×10^{-4}	3.14×10^{-4}	2.65×10^{-4}	2.76×10^{-4}	1.91×10^{-4}	1.83×10^{-4}	1.89×10^{-4}	4.74×10^{-5}	7.88×10^{-5}
^{36}Ar/^{40}Ar	0.00287	0.00110	0.00096	0.00124	0.00084	0.00184	0.00270	0.00298	0.00324	0.00310
Err. ^{36}Ar/^{40}Ar	8.42×10^{-6}	6.90×10^{-6}	7.36×10^{-6}	8.43×10^{-6}	5.39×10^{-6}	1.16×10^{-5}	9.08×10^{-6}	9.97×10^{-6}	9.65×10^{-6}	9.52×10^{-6}

Table 7

Table 8

MH-T4 muscovite										
Weight = 0.01516 g; J = 0.001006; [K] = 9.14 %; [Ca] = 630 ppm; [Cl] = 120 ppm; Err. = Error										
Step	1	2	3	4	5	6	7	8	9	10
T (°C)	745	765	783	804	827	857	892	948	1134	1310
^{40}Ar total	3.15×10^{-8}	6.32×10^{-9}	7.77×10^{-9}	7.11×10^{-9}	5.56×10^{-9}	7.46×10^{-9}	8.21×10^{-9}	8.56×10^{-9}	1.04×10^{-8}	9.50×10^{-9}
Err. ^{40}Ar	9.44×10^{-12}	1.28×10^{-12}	1.62×10^{-12}	1.92×10^{-12}	1.65×10^{-12}	3.37×10^{-12}	2.06×10^{-12}	1.92×10^{-12}	2.63×10^{-12}	2.16×10^{-12}
^{40}Ar×	1.37×10^{-9}	1.57×10^{-9}	4.40×10^{-9}	5.26×10^{-9}	4.16×10^{-9}	5.56×10^{-9}	6.02×10^{-9}	5.98×10^{-9}	6.38×10^{-9}	2.10×10^{-9}
^{39}Ar	3.34×10^{-10}	3.54×10^{-10}	1.00×10^{-9}	1.20×10^{-9}	9.49×10^{-10}	1.27×10^{-9}	1.37×10^{-9}	1.36×10^{-9}	1.44×10^{-9}	4.65×10^{-10}
Err. ^{39}Ar	5.21×10^{-13}	5.27×10^{-13}	9.24×10^{-13}	1.02×10^{-12}	8.52×10^{-13}	1.19×10^{-12}	1.10×10^{-12}	1.09×10^{-12}	1.17×10^{-12}	5.36×10^{-13}
% ^{39}Ar	3.43	3.64	10.29	12.33	9.73	13.04	14.09	13.92	14.75	4.77
^{38}Ar	8.95×10^{-11}	8.03×10^{-12}	1.42×10^{-11}	1.53×10^{-11}	1.20×10^{-11}	1.60×10^{-11}	1.75×10^{-11}	1.76×10^{-11}	1.97×10^{-11}	1.03×10^{-11}
Err. ^{38}Ar	1.29×10^{-13}	1.76×10^{-14}	2.59×10^{-14}	3.04×10^{-14}	2.39×10^{-14}	2.75×10^{-14}	3.17×10^{-14}	3.26×10^{-14}	3.73×10^{-14}	1.95×10^{-14}
^{38}Ar$_{Cl}$	6.68×10^{-11}	1.09×10^{-12}	9.02×10^{-13}	7.49×10^{-13}	5.84×10^{-13}	6.86×10^{-13}	8.82×10^{-13}	9.03×10^{-13}	1.20×10^{-12}	4.57×10^{-13}
^{37}Ar	1.55×10^{-11}	3.51×10^{-12}	2.48×10^{-12}	1.92×10^{-12}	1.44×10^{-12}	1.68×10^{-12}	1.41×10^{-12}	1.48×10^{-12}	2.67×10^{-12}	2.82×10^{-12}
Err. ^{37}Ar	8.05×10^{-14}	7.19×10^{-14}	7.17×10^{-14}	7.16×10^{-14}	7.10×10^{-14}	7.11×10^{-14}	7.11×10^{-14}	7.12×10^{-14}	7.14×10^{-14}	7.14×10^{-14}
^{36}Ar	1.01×10^{-10}	1.59×10^{-11}	1.13×10^{-11}	6.18×10^{-12}	4.68×10^{-12}	6.36×10^{-12}	7.34×10^{-12}	8.65×10^{-12}	1.34×10^{-11}	2.48×10^{-11}
Err. ^{36}Ar	2.72×10^{-13}	4.61×10^{-14}	3.45×10^{-14}	2.08×10^{-14}	1.76×10^{-14}	2.20×10^{-14}	2.56×10^{-14}	2.75×10^{-14}	4.01×10^{-14}	7.04×10^{-14}
Age	7.41	8.02	7.93	7.92	7.94	7.93	7.94	7.97	8.03	8.17
Err. age (1σ)	0.44	0.07	0.02	0.01	0.01	0.01	0.01	0.01	0.02	0.08
Ca/K	0.08990	0.01922	0.00480	0.00310	0.00293	0.00256	0.00198	0.00212	0.00360	0.01176
Err. Ca/K	0.00049	0.00039	0.00014	0.00012	0.00015	0.00011	0.00010	0.00010	0.00010	0.00030
Cl/K	0.03557	0.00055	0.00016	0.00011	0.00011	0.00010	0.00011	0.00012	0.00015	0.00018
Err. Cl/K	0.00007	0.00004	0.00001	0.00001	0.00001	0.00001	0.00001	0.00001	0.00001	0.00003
^{39}Ar/^{40}Ar	0.01061	0.05608	0.12912	0.16919	0.17063	0.17030	0.16728	0.15864	0.13876	0.04897
Err. ^{39}Ar/^{40}Ar	1.69×10^{-5}	8.42×10^{-5}	1.22×10^{-4}	1.51×10^{-4}	1.61×10^{-4}	1.77×10^{-4}	1.40×10^{-4}	1.32×10^{-4}	1.18×10^{-4}	5.75×10^{-5}
^{36}Ar/^{40}Ar	0.00320	0.00252	0.00145	0.00087	0.00084	0.00085	0.00089	0.00101	0.00129	0.00261
Err. ^{36}Ar/^{40}Ar	8.70×10^{-6}	7.31×10^{-6}	4.44×10^{-6}	2.93×10^{-6}	3.17×10^{-6}	2.97×10^{-6}	3.12×10^{-6}	3.22×10^{-6}	3.88×10^{-6}	7.44×10^{-6}

Table 8